Gondwana Research 38 (2016) 40–59

Contents lists available at ScienceDirect

Gondwana Research

journal homepage: www.elsevier.com/locate/gr

Geochronology and geochemistry of igneous rocks in the Bailingshan area: Implications for the tectonic setting of late Paleozoic magmatism and iron skarn mineralization in the eastern Tianshan, NW China

Weifeng Zhang [a,b], Huayong Chen [a,*], Jinsheng Han [a], Liandang Zhao [a,b], Jianhan Huang [a,b], Juntao Yang [c], Xuelu Yan [c]

[a] Key Laboratory of Mineralogy and Metallogeny, Guangzhou Institute of Geochemistry, Chinese Academy of Sciences, Guangzhou 510640, China
[b] University of Chinese Academy of Sciences, Beijing 100049, China
[c] No. 1 Geological Party Xinjiang Bureau of Geology and Mineral Exploration, Changji, 831100, China

ARTICLE INFO

Article history:
Received 2 May 2015
Received in revised form 23 October 2015
Accepted 31 October 2015
Available online 12 November 2015

Handling Editor: R. Goldfarb

Keywords:
Zircon U–Pb dating
Sr–Nd–Pb isotopes
Eastern Tianshan
Back-arc magmatism
Late Paleozoic

ABSTRACT

The late Paleozoic Bailingshan intrusions and volcanic rocks are located in the Aqishan–Yamansu arc belt in the southern part of the eastern Tianshan and are associated with an important group of iron skarn deposits. The exposed intrusive rocks are mainly granodiorite, monzonitic granite, and granite. Zircon U–Pb dating of the Tugutublak Formation tuffaceous dacitic lava yields an age of 324 Ma, whereas dates of the Bailingshan granodiorite, monzonitic granite, and granite yields ages of 317 Ma, 313 Ma, and 307 Ma, respectively. The results indicate that the Bailingshan granitoids were emplaced soon after the eruption of the Tugutublak dacite. All these rocks studied show calc-alkaline to high-K calc-alkaline and metaluminous affinities, with A/CNK values ranging 0.83–1.10. They are enriched in Rb, K, and Pb, depleted in Nb, Ta, Ti, and P, and contain low Sr/Y (4.16–23.7) and Sr (109.0–347.0 ppm) values, displaying typical arc geochemical affinities. The tuffaceous dacitic lava has low Nb/Ta (10.3–14.1) values, a wide range of $Mg^{\#}$ (6–64), positive zircon $\varepsilon_{Hf}(t)$ (3.2–7.5) values, and elevated whole-rock $\varepsilon_{Nd}(t)$ (2.03–4.41), but low I_{Sr} values (0.70427–0.70530), indicating that the source magma may have been derived from the juvenile lower crust with minor mantle input. The Bailingshan I-type intrusions also exhibit a mixed source signal, as constrained by Nb/Ta ratios, $Mg^{\#}$, and isotopes characteristics. Because the granodiorite, monzonitic granite, and granite intrusions have higher zircon $\varepsilon_{Hf}(t)$ (3.3–7.5, 11.8–13.5, and 10.2–14.4, respectively) and $\varepsilon_{Nd}(t)$ (3.90, 5.78, and 5.94, respectively) values than those of the tuffaceous dacitic lava, it is suggested that mantle-derived materials may have played a more prominent role with their petrogenetic evolution. Integrating our new geological, age, geochemical and isotopic data we propose that the Aqishan–Yamansu iron skarn belt may have formed in a back-arc position or within an intra-arc basin generated by the southward subduction of the Kanggur oceanic plate beneath the Yili–Central Tianshan block during the late Paleozoic, with felsic-intermediate magmatism occurring during the basin inversion.

© 2015 International Association for Gondwana Research. Published by Elsevier B.V. All rights reserved.

1. Introduction

The Central Asian Orogenic Belt (CAOB) is sandwiched between the European and Siberian cratons in the north and the Tarim and North China cratons in the south (Sengör et al., 1993; Xiao et al., 2004; Windley et al., 2007; Xiao et al., 2008, 2009, 2013). This orogenic belt is commonly accepted as a Neoproterozoic to Permian giant accretionary orogen that experienced oceanic plate subduction and terrane accretion episodes, with final ocean closure occurring during the Late Carboniferous to Early Permian (Sengör and Natal'in, 1996; Chen, 2000; Chen and Jahn, 2004; Xiao et al., 2008). As an important component of the CAOB, the Tianshan Orogenic Belt (TOB), is the suture zone between the Tarim craton and Junggar block (Chen, 2000; Chen and Jahn, 2004; Xiao et al., 2004, 2008, 2009) (Fig. 1a), with the eastern TOB (i.e., Eastern Tianshan) comprising several tectonic units bounded by nearly EW-trending faults (Xiao et al., 2004; Mao et al., 2005; Xiao et al., 2008, 2009). These tectonic units include, from north to south, the Dananhu–Tousuquan arc, the Kanggur shear zone, and the Aqishan–Yamansu arc belt (Fig. 1b). The Aqishan–Yamansu belt also is the host for one of the most important metallogenic belts in northwestern China, a belt that includes numerous high-grade Fe deposits, including, from west to east, the Aqishan, Hongyuntan, Bailingshan, Duotoushan, Yamansu, and Shaquanzi deposits (Wang et al., 2005; Wang et al., 2006; Zhang and Zhang, 2012; Zhang et al., 2012; Huang et al., 2013; Hou et al., 2014). These Fe skarn deposits are commonly hosted in submarine volcanic and sedimentary rocks of the Tugutublak Formation, with extensive skarn development but a general lack of

* Corresponding author.

http://dx.doi.org/10.1016/j.gr.2015.10.011
1342-937X/© 2015 International Association for Gondwana Research. Published by Elsevier B.V. All rights reserved.

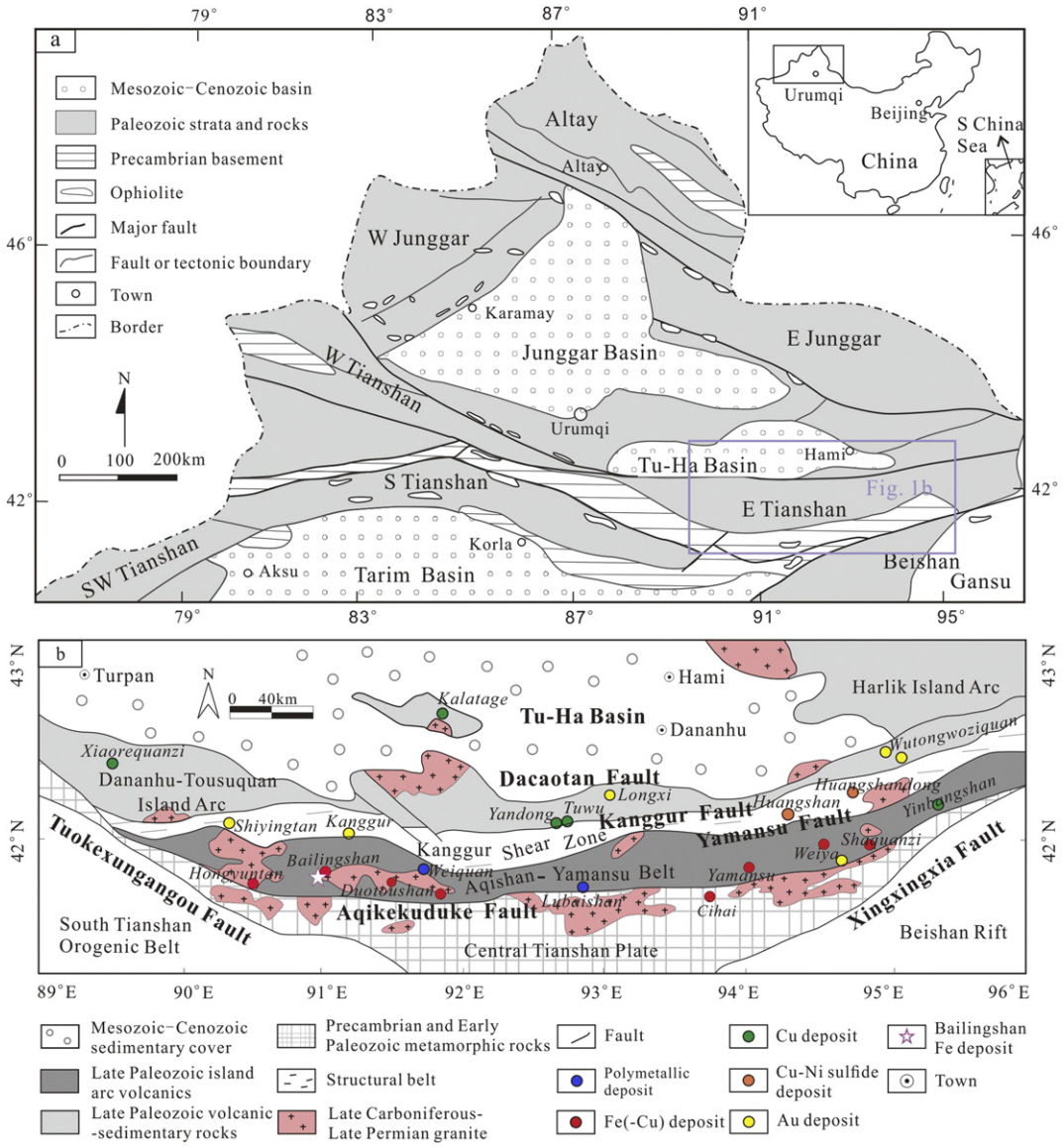

Fig. 1. (a) Location of the eastern Tianshan in the Central Asian Orogenic Belt (modified after Chen et al., 2012). (b) Geologic map of the eastern Tianshan (modified after Mao et al., 2005; Wang et al., 2006).

direct contact relationship between intrusions and the skarn and iron ores (Mao et al., 2005; Wang et al., 2005; Wang et al., 2006; Pirajno et al., 2011; Zhang and Zhang, 2012; Zhang et al., 2012). The widespread Carboniferous granitoids and marine volcanic-sedimentary rocks have attracted significant attention in the last two decades, in large part, because of the economic iron deposits (C.Z. Wu et al., 2006; Zhou et al., 2010; Lei et al., 2013; Hou et al., 2014). However, the geodynamic setting of these Fe deposits and their spatially associated igneous rocks remains controversial relative to the majority of the arc. Various proposed hypotheses include local magmatism and ore formation in a southward subduction-related back-arc basin (Hou et al., 2014), northward subduction-related island arc (Yang et al., 1996; Xiao et al., 2004; Han et al., 2014), and bipolar subduction-related island arc (J.Y. Li et al., 2002, 2006; Wang et al., 2014). In addition, petrogenesis and geochronology of the Tugutublak Formation, one of the most important ore-bearing strata, remain unclear.

The Bailingshan Fe deposit is one of the important iron skarn deposits in the western part of the Aqishan–Yamansu arc belt. Since its discovery in the 1990s, preliminary investigations were carried out to describe its geology (Li and Li, 1999; Wang et al., 2005; Meng et al., 2013). Zhou et al. (2010) reported a zircon U–Pb age of 317.7 ± 3.5 Ma for the Bailingshan granodiorite that is 1.5 km from the deposit. Nevertheless, critical geological issues, including detailed geochemical features and the possible magma source(s) of the Bailingshan granodiorite remain poorly understood. Moreover, the ages and geochemical signature of the other intrusive rocks in the deposit area (i.e., the Bailingshan granite and monzonitic granite) are yet to be well-constrained. This inhibits the establishment of a genetic model for the Bailingshan Fe deposit. In this contribution, we present new zircon U–Pb ages, and isotopic and whole-rock geochemical data for the Bailingshan granitoids, as well as the first detailed study on the ore-bearing Tugutublak Formation tuffaceous dacitic lava. Comparing the Bailingshan geology with the Mesozoic back (intra)-arc setting in the Andes, we synthesize a new tectonic model for a part of the Aqishan–Yamansu arc belt and its associated belt of iron deposits.

2. Geological setting

2.1. Regional geology

The eastern Tianshan region is an approximately 300 km wide orogenic collage that is bounded by the Junggar block to the north and

the Tarim craton to the south (Fig. 1a; Chen et al., 2012). The northern Dananhu–Tousuquan arc is situated between the Kanggur and Dacaotan Fault (Fig. 1b), and mainly composed of Devonian to Jurassic sedimentary-volcanic rocks and Cenozoic sediment covers. The Devonian Dananhu Formation contains basaltic to andesitic volcanic rocks, whereas the Lower Carboniferous Gandun Formation is composed dominantly of turbidites with minor limestone and volcanic rocks. Overlying these arc-related rocks are those of the upper Carboniferous Qi'eshan Formation, consisting of basalt, andesite, spilite, keratophyre, andesitic brecciated lavas, lithic sandstone, pebbly lithic sandstone, and conglomerate. The Qi'ershan Formation, in turn, is overlain by the Permian basalt, tuff, and volcanic breccia, and Jurassic terrestrial clastic rocks (Qin et al., 2002, 2003; Xiao et al., 2004; Mao et al., 2005). Intrusions were widely emplaced in the arc during the Devonian to Carboniferous, with several important Carboniferous porphyry Cu deposits (e.g., Tuwu–Yandong) formed along this belt. Molybdenite Re–Os dating yielded a well-constrained ^{187}Re–^{187}Os isochron age of 323 ± 2 Ma for the porphyry deposits (Rui et al., 2002).

The middle Kanggur shear zone lies between the Kanggur and Yamansu faults, and major strata in this shear zone are the Early Carboniferous volcano-sedimentary rocks in the south, and mélanges with broken formations in the north (Xiao et al., 2013). Abundant ophiolitic fragments (Li et al., 2006), with extensive Permian mafic and ultramafic intrusions (e.g., at Xiangshan, Huangshandong, Huangshan and Hulu) are present in the eastern section of the belt (Qin, 2000; Zhou et al., 2004; Mao et al., 2005; Han et al., 2010). Zircon U–Pb dating yielded ages of 269 ± 2 Ma (Zhou et al., 2004), 274 ± 3 Ma (Han et al., 2010), and 285 ± 1.2 Ma (Qin, 2000) for the Huangshan, Huangshandong, and Xiangshan mafic / ultramafic intrusions, respectively. The Kanggur shear zone contains a series of epithermal Au, orogenic Au, and magmatic Cu–Ni sulfide deposits formed at ca. 290–250 Ma (Mao et al., 2005; Yang et al., 2009; Pirajno et al., 2011).

The Aqishan–Yamansu arc belt, located between the Yamansu Fault and the Aqikekuduke Fault in the south (separating the belt from the Central Tianshan Plate), contains mainly two marine units. These include rocks of the Yamansu Formation that are mainly distributed in the northern part of the Aqishan–Yamansu belt, and rocks of the Tugutublak Formation exposed in the southern part; they are separated by an unnamed E–W-trending deep-seated fault (Muhetaer et al., 2014). The 5-km-thick Early Carboniferous bimodal volcanic succession (i.e., the Yamansu Formation) can be subdivided into three members based on lithologies (Fig. 2). The basal member contains greenish-gray mafic to intermediate tuff, volcanic breccia, and medium- to fine-sandstone with minor bioclastic limestone intercalation. The middle member is dominated by felsic tuff, coarse sandstone, and mixtite, intercalated with bioclastic limestone and microcrystalline limestone. The uppermost member contains limestone, with minor tuff and sandstone (Qin et al., 2002; Zhang et al., 2012; Hou et al., 2014). Some index fossils, such as Arachnolasma, Gigantoprductus, and Yuanophyllum, are present in this layer (Zhang et al., 2012). The Late Carboniferous strata (i.e., the Tugutublak Formation, also known as the Matoutan Formation (Wang et al., 2005) or the Shaquanzi Formation (Mao et al., 2005)) are also subdivided into three units. The lowermost unit, containing mainly aubergine andesite, rhyolite flows, crystal tuff, and tuffaceous lava, and intercalated with volcanic breccia, agglomerate, limestone, and sandstone, unconformably overlies rocks of the Yamansu Formation. On top of the lowermost unit are the volcanic breccia, tuff, sandstone, and limestone of the middle member. The uppermost member comprises mainly purplish-gray andesite and gray basaltic lava interbedded with minor aubergine rhyolite and sandstone. Fossils such as corals and fusulinids are located in the intercalated limestone (Zhang et al., 2012). Numerous arc-related late Paleozoic granitoids have intruded rocks of the above two marine units (C.Z. Wu et al., 2006; Zhou et al., 2010). They include the Hongyuntan granodiorite (328.5 ± 9.3 Ma), Bailingshan granodiorite (317.7 ± 3.7 Ma), Xifengshan granite (349 ± 3.4 Ma), Weiquan granodiorite (297 ± 3 Ma), and Longdong monzonitic granite (276.2 ± 2.5 Ma). Minor Triassic granitoids were emplaced in a subsequent post-collision setting and are represented by the Tudun granite (246.2 ± 2.6 Ma; Zhou et al., 2010) and Yamansubei granite (227.9 ± 0.47 Ma; Lei et al., 2013).

Mineral deposits in the Aqishan–Yamansu belt have been assigned to four major types (Fig. 1b): (1) Fe skarn deposits, (2) Fe–Cu deposits, (3) Cu–Ag–Pb–Zn skarn deposits, and (4) Cu-rich VMS deposits (Mao et al., 2005; Wang et al., 2006; Pirajno et al., 2011). The Fe skarns include those at Aqishan, Hongyuntan, Bailingshan, Chilongfeng, and Yamansu, whereas Fe–Cu deposits are represented by the Duotoushan, Heifengshan, Shuangfengshan and Shaquanzi. As the largest Fe deposit in the arc belt, the Yamansu deposit contains 32 Mt at 51% Fe (Mao et al., 2005). Hou et al. (2014) proposed that the Yamansu skarn and other iron-rich ore deposits were formed by interaction of magmatic water and seawater with submarine volcanic and sedimentary rocks of Yamansu Formation. Huang et al. (2013) reported ^{187}Re–^{187}Os isochron ages for pyrite from the Hengfengshan (312 ± 23 Ma), Shuangfengshan (294.5 ± 7.2 Ma) and Shaquanzi (295.2 ± 7.3 Ma) Fe–Cu skarn deposits. Those Cu–Ag–Pb–Zn skarns are exemplified by the Weiquan deposit that is hosted in felsic volcanic and carbonate rocks of the Tugutublak Formation, with a fairly well constrained U–Pb SHRIMP age of ca. 290–280 Ma and a $^{39}Ar/^{49}Ar$ age of ca. 277 Ma determined on skarn amphiboles (Pirajno et al., 2011). The Cu-rich Yinbangshan VMS Cu-rich deposit, hosted in rocks of the Yamansu Formation, has not been dated (Wang et al., 2006; Li et al., 2012), but must be syngenetic with its Early Carboniferous host rocks and thus older than the belt of Late Carboniferous–Permian skarns.

2.2. Deposit geology

The Bailingshan Fe deposit occurs at about 144 km southeast of Shanshan City. The exposed strata are the Late Carboniferous Tugutublak Formation dacitic tuff, andesitic tuffaceous breccia, tuffaceous andesitic-dacitic lava, and andesitic tuff/tuffaceous breccia from the bottom to top. There are no carbonate rocks occurring in the deposit area (Wang et al., 2005). The volcanic–sedimentary strata in the area have been intruded by many granitoids, including granodiorite, granite, and granite porphyry. However, orebodies are mainly hosted in the volcanic rocks and granitoids are generally at least 500 m from any intrusions exposed at the surface (Wang et al., 2005; Fig. 3). The granite porphyry was not observed in our investigation of the deposit, but monzonitic granite was newly identified in drill cores. We also noted several mafic dikes that cut the Fe orebodies (Fig. 4a). At least six sets of faults, mainly NE-, EW-, and NW-trending, have been recognized in the deposit area (Fig. 3).

The Bailingshan Fe deposit contains a reserve of 13.065 Mt Fe ore with an average grade of 44.94%. Since 1999, it has produced 1.5 Mt Fe mainly from underground mining. Three stratiform orebodies have been recognized in the deposit. The No. I orebody (600-m-long, averages 3.38 m in width, and dips NE at 25° to 35°) is the largest and most productive, containing about 50% of the total reserves (Wang et al., 2005; Zhang and Zhang, 2012). The Bailingshan orebodies are hosted in the andesitic tuffaceous breccia of the Tugutublak Formation, and are mostly conformable with their country rocks (Fig. 4b).

Ore textures are mainly massive or disseminated. Field and petrographic observation indicate that ore minerals at Bailingshan are dominated by magnetite and hematite, with minor pyrite and chalcopyrite, whereas gangue minerals include mainly garnet, clinopyroxene, amphibole, epidote, chlorite, quartz, and calcite. Paragenesis of alteration at Bailingshan has been recognized on the basis of mineral assemblages and textural relationships (Fig. 4). Lighter brown to yellow-green garnet and dark-green amphibole with minor clinopyroxene were overprinted by magnetite, an event that brecciated the earlier skarn (Fig. 4c). Magnetite in the disseminated mineralization is associated with epidote, minor amphibole, and sulfides (Fig. 4d). Anhydrous minerals (e.g., garnet, clinopyroxene) are entirely or partially replaced by

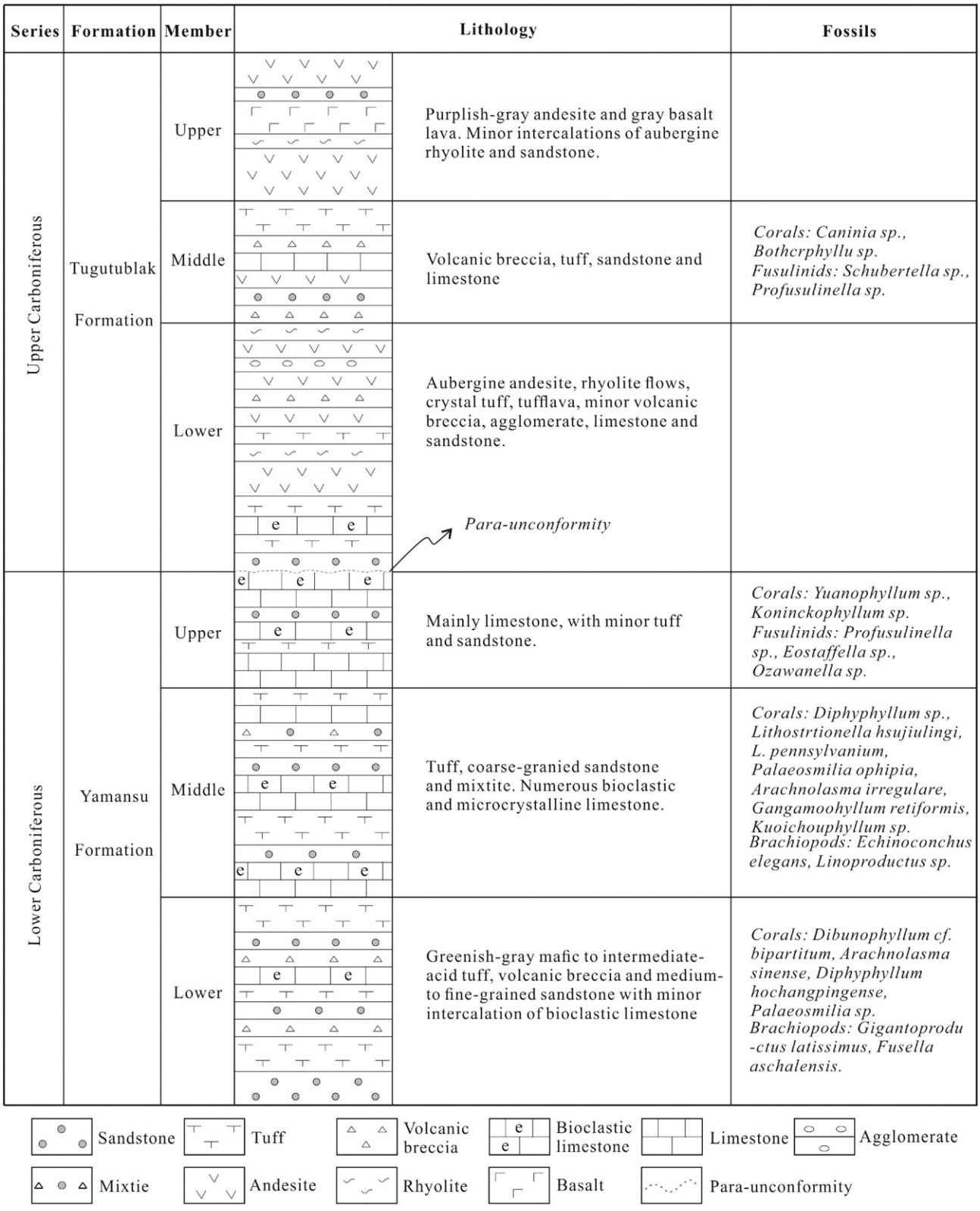

Fig. 2. Summarized stratigraphic column for the Lubaishan–Bailingshan district in the Aqishan–Yamansu belt (modified after Zhang et al., 2012).

amphibole and epidote (Fig. 4e, f). Extensive replacement of early amphibole by epidote and magnetite is common (Fig. 4g, h), suggesting that amphibole was largely formed prior to epidote and magnetite. Late-stage hydrothermal veins are abundant at Bailingshan, such as fine-grained subhedral quartz veins cutting magnetite (Fig. 4i). Our paragenesis study indicates that early anhydrous mineral assemblages were overprinted by later hydrous retrograde minerals and magnetite mineralization is mainly associated with this retrograde alteration.

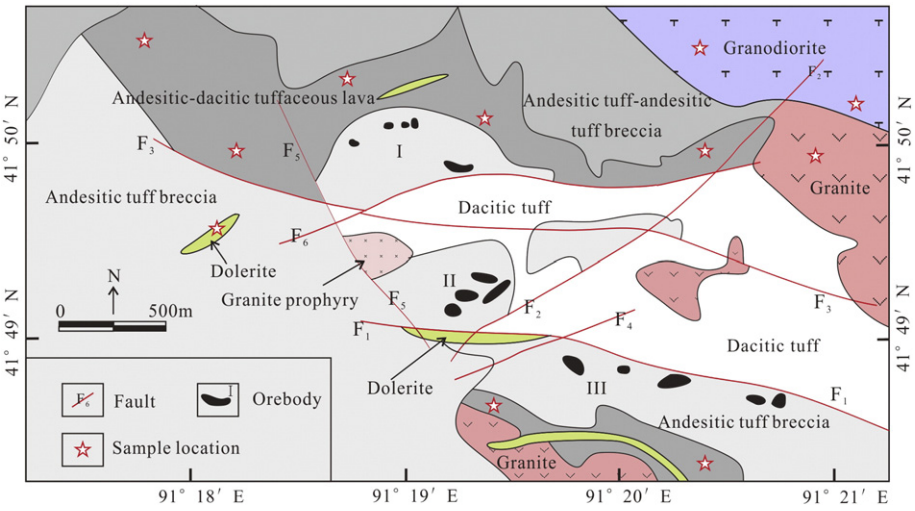

Fig. 3. Geologic map of the Bailingshan Fe deposit (modified form Wang et al., 2005).

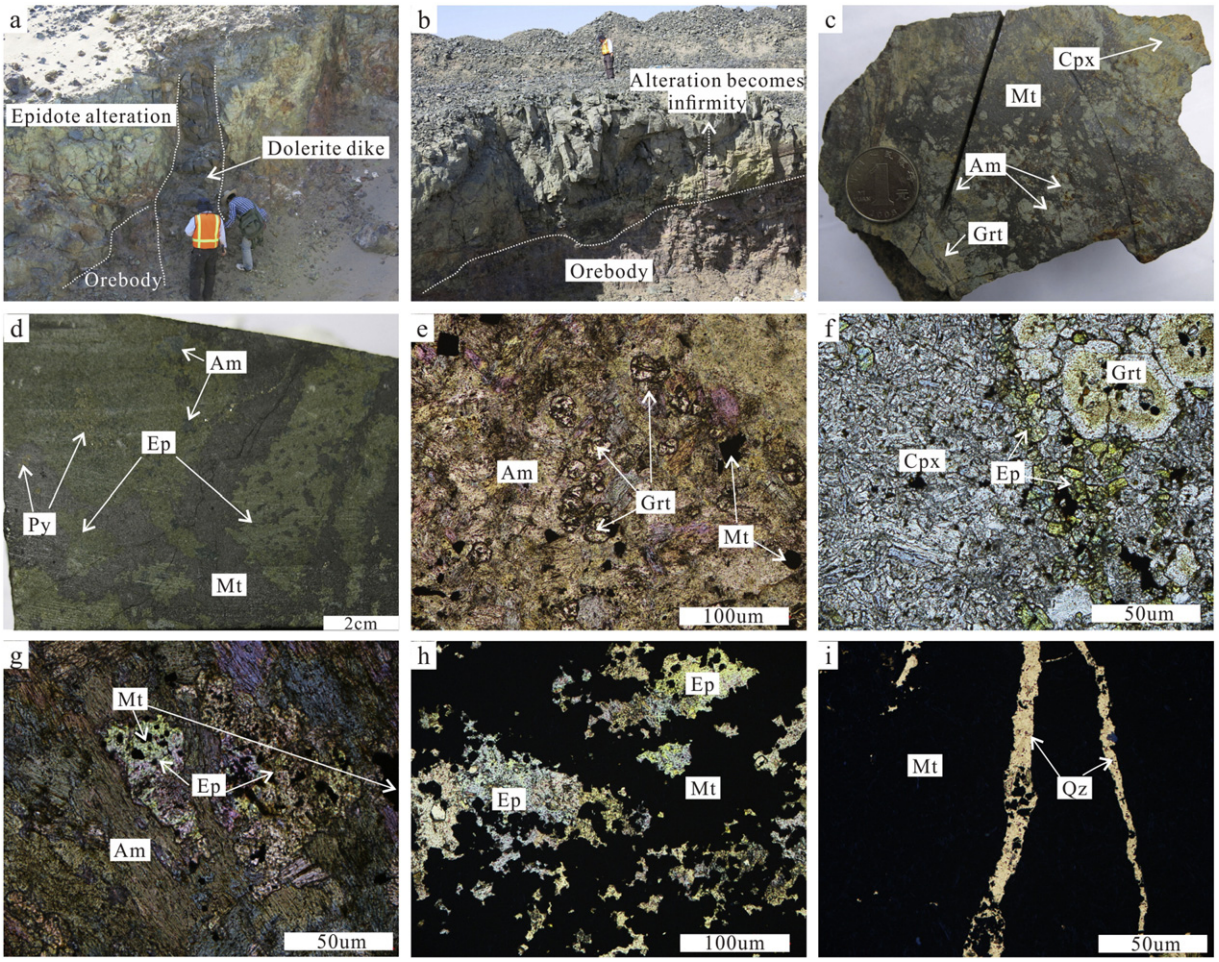

Fig. 4. Representative photographs showing mineral assemblages and textural features from the Bailingshan deposit. (a) Dolerite dike cutting the epidote alteration and Fe orebodies. (b) The Bailingshan orebodies are mostly conformable with their country rocks, with wall rock alteration intensity fading away from the orebodies. (c) Garnet and amphibole with minor clinopyroxene overprinted by magnetite, and formed the hydrothermal breccia. (d) Epidote coexists with magnetite. (e) Garnet overprinted by amphibole; plane-polarized light. (f) Euhedral–subhedral garnet and clinopyroxene (partially) replaced by epidote; plane-polarized light. (g) Magnetite and green epidote overprinted the euhedral amphibole; plane-polarized light. (h) Coexisting magnetite and epidote; plane-polarized light. (i) Quartz veinlets cut the magnetite; plane-polarized light. Abbreviations: Am = amphibole, Cpx = clinopyroxene, Ep = epidote, Grt = garnet, Mt = magnetite, Py = pyrite, Qz = quartz.

Fig. 5. Hand specimen and microscopic photos of rocks from the Bailingshan area. (a)–(b) BL-004, tuffaceous dacitic lava; (c)–(d) BL-065, granodiorite; (e)–(f) BL-058, monzonitic granite; (g)–(h) BL-050, granite; (i)–(j) Bl-037, dolerite. Abbreviations: Bt = biotite, Hb = hornblende, Kfs = K-feldspar, Opx = orthopyroxene, Pl = plagioclase, Qz = quartz.

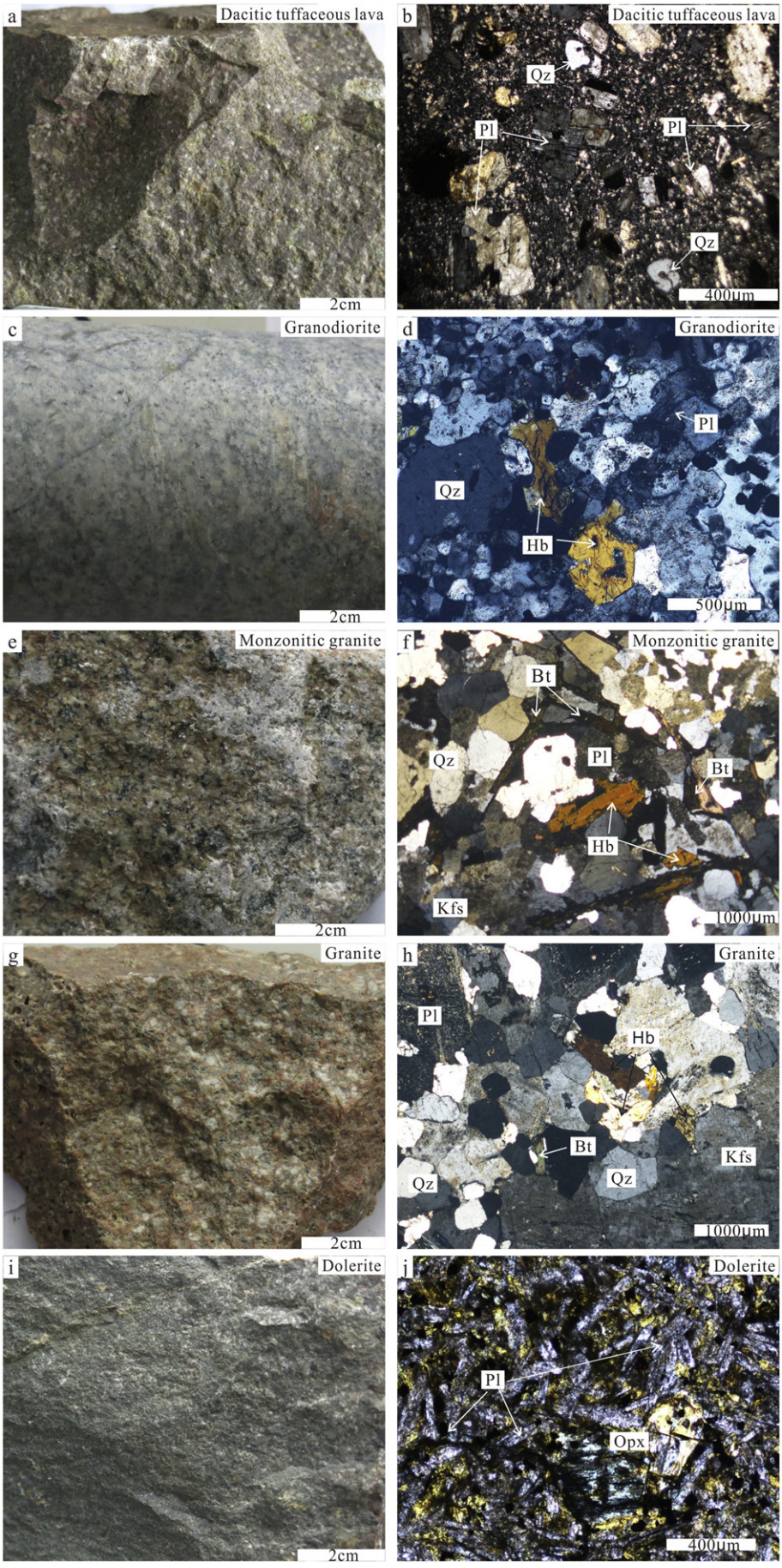
a
Dacitic tuffaceous lava
2cm
b
Dacitic tuffaceous lava
Qz
Pl
Pl
Qz
400μm
c
Granodiorite
2cm
d
Granodiorite
Pl
Qz
Hb
500μm
e
Monzonitic granite
2cm
f
Monzonitic granite
Bt
Qz
Pl
Bt
Hb
Kfs
1000μm
g
Granite
2cm
h
Granite
Pl
Hb
Bt
Kfs
Qz
Qz
1000μm
i
Dolerite
2cm
j
Dolerite
Pl
Opx
400μm

3. Sampling and petrography

Following detailed geological sampling, fourteen relatively fresh igneous rock samples were chosen for analyses. The analyzed samples include tuffaceous dacitic lava, granitoids and dolerite dikes. Petrographic evidence suggests that these rocks had undergone low-grade metamorphism and minor hydrothermal alteration.

Tuffaceous dacitic lava from the Tugutublak Formation has porphyritic texture, containing a glassy groundmass with microlites of plagioclase and minor quartz (Fig. 5a–b). Intrusions include granodiorite, monzonitic granite, and granite. The granodiorites contain mainly plagioclase (30%), quartz (40%), K-feldspar (10%), hornblende (10%), and biotite (5%), with minor (<5%) apatite, sphene, and magnetite (Fig. 5c–d). The monzonitic granites are composed mainly of plagioclase (30%), K-feldspar (25%), quartz (25%), biotite (10%), hornblende (5%), and minor apatite and magnetite (Fig. 5e–f). The granites are pink and have more plagioclase and hornblende than the monzonitic granites, and consist of K-feldspar (35%), plagioclase (25%), quartz (20%), biotite (5%), hornblende (8%), and accessory minerals such as zircon, apatite, and magnetite (Fig. 5g–h). All primary minerals of the studied granitoid rocks are fine- to medium-grained. The dolerite contains euhedral plagioclase, pyroxene, and minor magnetite (Fig. 5i–j). The pyroxene was partially altered to chlorite and epidote.

4. Analytical methods

4.1. Major and trace elements analysis of whole rock

Whole-rock major and trace elements analysis was performed at the ALS Chemex Company in Guangzhou, China. All the samples were first powdered to less than 200-mesh, then added to Lithium Borate Flux (50%–50% $Li_2B_4O_7$–$LiBO_2$), mixed well and fused in an auto fluxer between 1050 °C and 1100 °C. The major elements were analyzed by X-ray fluorescence spectrometry, and the analytical precision is better than 1%.

For trace elements, including rare earth elements (REE), the prepared samples (50 mg of powder) are added to lithium metaborate flux, mixed well, and fused in a furnace at 1000 °C. The resulting melt was then cooled and dissolved in 100 ml of 4% HNO_3. This solution is then analyzed by inductively coupled plasma-mass spectrometry (ICP-MS) for trace elements. The analytical precision is better than ±5% for most trace elements. The analytical results are presented in Table 1.

4.2. Zircon U–Pb geochronology and in-situ Hf isotopes

Zircons were separated by the standard density and magnetic separation techniques, and then hand-picked under a binocular microscope. Zircon internal structure was studied via cathodoluminescence (CL) imaging using a JXA-8100 Electron Probe Microanalyzer with a Mono CL3 Cathodoluminescence System for high resolution imaging and spectroscopy at the Guangzhou Institute of Geochemistry, Chinese Academy of Sciences (GIGCAS).

Laser Ablation-ICP-MS zircon U–Pb dating for the majority of samples (BL-004, BL-050, BL-058 and Bl-065) were performed in the State Key Laboratory of Isotope Geochemistry, GIGCAS. Before the analysis, each sample's surface was cleaned with ethanol to eliminate possible contamination. Each analysis incorporated a background acquisition of approximately 20–30 s followed by 50 s of data acquisition from the sample. The NIST SRM 610 glass and Temora zircon standards were used as external standards. Each block of five unknown samples was bracketed by analyses of standards. Off-line inspection and integration of background and analysis signals, and time-drift correction and quantitative calibration for trace element analyses and U–Pb dating were performed using ICPMSDataCal (Liu et al., 2008). Age calculation and plotting of concordia diagrams were performed using Isoplot/Ex 3.0 (Ludwig, 2003). The detailed analytical techniques were described by Li et al. (2011) and the analytical results are presented in Table 2.

Zircon Lu–Hf isotopic analyses were performed using a Nu Plasma HR MC-ICP-MS (Nu Instruments, UK), coupled to a 193 nm excimer laser ablation system (RESOlution M-50, Resonetics LLC, USA) in the State Key Laboratory of Isotope Geochemistry, GIGCAS. The measured isotopic ratios of $^{176}Hf/^{177}Hf$ were normalized to $^{179}Hf/^{177}Hf = 0.7325$, using exponential correction for mass bias. The in-situ measured $^{173}Yb/^{172}Yb$ ratio was used for mass bias correction for both Yb and Lu because of their similar physicochemical properties. Ratios used for the corrections were 0.5886 for $^{176}Yb/^{172}Yb$ (Chu et al., 2002) and 0.02655 for $^{176}Lu/^{175}Lu$ (Machado and Simonetti, 2001). The measured $^{176}Lu/^{177}Hf$ ratios and the ^{176}Lu decay constant of 1.867×10^{-11} year^{-1} reported by Soderlund et al. (2004) were used to calculate initial $^{176}Hf/^{177}Hf$ ratios. Chondritic values of $^{176}Hf/^{177}Hf = 0.0336$ and $^{176}Lu/^{177}Hf = 0.282785$ reported by Bouvier et al. (2008) were used for the calculation of $\varepsilon_{Hf}(t)$ values. The depleted mantle line is defined by present-day $^{176}Hf/^{177}Hf = 0.28325$ and $^{176}Lu/^{177}Hf = 0.0384$ (Griffin et al., 2004). Single-stage Hf model ages (T_{DM}) were calculated relative to the depleted mantle which is assumed to have linear isotopic growth from $^{176}Hf/^{177}Hf = 0.279718$ at 4.55 Ga, to 0.283250 at present, with a $^{176}Lu/^{177}Hf = 0.0384$ (Griffin et al., 2004), and two-stage Hf model ages (T_{DM}) were calculated assuming a mean $^{76}Lu/^{177}Hf$ value of 0.015 for the average continental crust (Griffin et al., 2002). The Lu–Hf isotopic data are listed in Table 2.

4.3. Whole-rock Sr–Nd–Pb isotopes

Whole-rock Sr–Nd–Pb isotopic analyses were performed using a Micromass Isoprobe Multi-Collector ICPMS at the State Key Laboratory of Isotope Geochemistry, GIGCAS. For Sr–Nd isotopic analyses, sample powders (~100 mg) were dissolved in distilled HF-HNO_3 Savillex screwtop Teflon beakers at 150 °C overnight. Strontium and REE were separated on columns made of Sr and REE resins from the Eichrom Company using 0.1% HNO_3 as an eluant. Separation of Nd from the REE fractions was carried out on HDEHP columns with a 0.18 N HCl eluant. Measured Sr and Nd isotopic ratios were normalized using a $^{86}Sr/^{88}Sr$ value of 0.1194 and a $^{146}Nd/^{144}Nd$ value of 0.7219, respectively. Analyses of standards NIST SRM, and Jndi-1 over the measurement period provided $^{87}Sr/^{86}Sr = 0.710291 \pm 6$ (2σ), and $^{143}Nd/^{144}Nd = 0.512084 \pm 3$ (2σ), respectively. Details of Sr, Nd, and Pb isotopic analytical methods are similar to those of Wei et al. (2002) and Liang et al. (2003).

For Pb analyses, ~200 mg of powder were dissolved in concentrated HF for three days. Lead was separated and purified by conventional cation-exchange techniques (200–400 mesh AG1X8 resin) with diluted HBr as the eluant. Analyses of standard NBS981 during the period of analysis provided results of $^{206}Pb/^{204}Pb = 16.9319 \pm 3$, $^{207}Pb/^{204}Pb = 15.4849 \pm 3$, and $^{208}Pb/^{204}Pb = 36.6781 \pm 11$.

5. Results

5.1. Whole-rock major and trace elements

Whole-rock major element, trace element, and REE analyses on the Bailingshan granitoids (granodiorite, monzonitic granite and granite) and tuffaceous dacitic lava are listed in Table 1. The Zr/TiO_2 vs. Nb/Y (Winchester and Floyd, 1976) and TAS (Wilson, 1989) diagrams were chosen for lithological classification. The tuffaceous dacite samples fall in the rhyodacite/dacite field, whereas the granitoid samples plot in the granodiorite and granite fields (Fig. 6a–b). The tuffaceous dacite exhibits a wide range of K_2O/Na_2O ratios (0.13–1.28), and fall mostly in the calc-alkaline field on the Th/Yb vs. Ce/Yb diagram (Fig. 7a). Compared with the dacite, K_2O/Na_2O ratios of the granodiorite, monzonitic granite and granite range from 0.23–1.23, 0.48–1.00, and 0.56–1.01, respectively. On the K_2O vs. Na_2O diagram (Fig. 7b), all the granitoids fall

Table 1
Whole-rock major- (wt.%), trace- (ppm) and rare earth (ppm) element compositions of representative rock samples from the Bailingshan area.

Rock types	Tuffaceous dacitic lava										Granite		
	BL-004	BL-008	BL-009	BL-013	BL-015	BL-016	BL-017	BL-019	BL-020	BL-050	D002	D005	D026
SiO_2	72.22	58.57	72.04	75.26	73.39	71.58	69.34	71.09	74.34	71.20	70.11	75.03	76.27
Al_2O_3	13.50	15.96	11.55	12.27	12.59	14.11	14.72	12.94	12.51	14.91	14.23	14.43	12.08
K_2O	5.03	1.91	2.40	0.78	2.49	1.75	2.72	0.97	2.43	3.97	3.32	3.30	2.60
Na_2O	3.93	5.87	4.40	5.88	4.89	5.68	3.60	5.85	5.29	4.20	4.79	3.27	4.61
CaO	1.51	3.62	1.77	1.80	2.02	2.35	2.55	1.81	0.64	1.92	3.12	1.91	1.29
$Fe_2O_3^T$	2.41	8.55	4.60	2.97	2.60	1.96	3.03	3.87	2.63	2.03	2.12	1.28	1.14
MgO	0.43	2.72	0.12	0.13	0.15	1.07	2.32	0.73	0.80	0.50	1.16	0.50	0.21
MnO	0.05	0.15	0.03	0.02	0.03	0.06	0.06	0.05	0.05	0.03	0.04	0.04	0.07
P_2O_5	0.06	0.12	0.07	0.05	0.07	0.08	0.09	0.07	0.05	0.05	0.09	0.06	0.03
TiO_2	0.34	0.71	0.36	0.28	0.37	0.44	0.48	0.39	0.37	0.21	0.02	0.06	0.16
LOI	0.49	0.85	1.31	0.45	0.89	0.75	1.02	0.73	0.53	1.13	0.47	0.39	0.34
Total	100.10	99.08	98.69	99.91	99.56	99.90	100.00	98.54	99.70	100.25	100.12	100.66	99.22
A/CNK	0.92	0.87	0.88	0.89	0.87	0.91	1.09	0.93	1.00	1.01	0.83	1.16	0.95
A/NK	1.13	1.36	1.17	1.17	1.17	1.25	1.66	1.21	1.10	1.33	1.24	1.61	1.16
$Mg^{\#}$	29	43	6	9	12	56	64	31	41	36	56	48	30
Rb	127.00	67.20	64.90	23.40	58.00	36.60	89.20	24.00	43.80	99.40			
Ba	1020.00	160.00	320.00	80.00	420.00	440.00	400.00	180.00	520.00	680.00			
Th	10.30	3.70	4.50	7.40	4.50	5.10	4.90	4.80	5.50	8.20			
U	2.90	1.00	1.50	2.60	2.80	1.80	1.50	2.20	1.50	1.30			
Nb	6.50	5.20	4.50	5.90	4.20	4.80	4.00	4.60	4.30	2.60			
Ta	0.63	0.37	0.33	0.49	0.33	0.38	0.32	0.33	0.34	0.23			
La	11.60	11.30	7.80	12.10	12.30	7.40	6.40	10.30	9.90	11.60			
Ce	24.50	25.20	17.30	25.10	25.40	17.40	15.95	23.10	23.40	26.00			
Pb	9.40	7.00	2.60	1.60	1.30	1.80	1.50	1.30	2.80	7.50			
Pr	2.85	3.05	2.06	3.00	2.90	2.13	2.01	2.84	2.89	2.99			
Sr	212.00	258.00	129.00	137.50	216.00	195.50	190.00	149.50	109.00	212.00			
Nd	11.10	12.70	8.60	11.80	11.70	9.40	8.70	12.10	12.20	11.80			
P	280.00	530.00	300.00	210.00	300.00	350.00	360.00	300.00	220.00	220.00			
Sm	2.58	3.31	2.11	2.95	2.71	2.75	2.32	3.28	3.12	2.83			
Zr	140.00	75.90	114.00	96.80	139.00	157.00	178.00	142.50	184.50	44.00			
Hf	4.00	2.30	3.20	2.90	4.00	4.50	5.10	3.90	5.10	1.80			
Eu	0.39	0.98	0.52	0.83	0.75	0.68	0.56	0.75	0.48	0.75			
Gd	2.68	3.66	2.39	3.09	2.85	3.63	2.62	3.78	3.42	2.88			
Tb	0.47	0.63	0.44	0.50	0.49	0.70	0.41	0.69	0.59	0.48			
Dy	3.13	3.99	3.08	3.20	3.35	5.07	2.57	4.83	4.02	3.07			
Y	19.80	23.10	21.30	19.50	20.40	32.60	16.60	29.40	26.20	18.60			
Ho	0.73	0.87	0.75	0.69	0.78	1.19	0.59	1.06	0.91	0.66			
Er	2.44	2.67	2.59	2.23	2.47	3.80	2.08	3.31	3.00	2.03			
Tm	0.38	0.38	0.41	0.34	0.37	0.56	0.34	0.48	0.46	0.30			
Yb	2.97	2.67	3.06	2.56	2.73	3.94	2.70	3.33	3.36	2.24			
Lu	0.50	0.42	0.49	0.42	0.45	0.61	0.49	0.51	0.57	0.36			
Co	1.70	15.80	108.50	25.70	1.10	2.20	4.60	2.70	2.60	1.90			
Ni	2.50	8.20	2.70	2.20	1.60	1.90	2.50	1.90	1.90	1.50			
Cr	45.00	34.00	50.00	57.00	38.00	49.00	27.00	45.00	59.00	25.00			
$(La/Yb)_N$	2.80	3.04	1.83	3.39	3.23	1.35	1.70	2.22	2.11	3.71			
$(Tb/Yb)_N$	0.72	1.07	0.65	0.89	0.82	0.81	0.69	0.94	0.80	0.97			
$(La/Sm)_N$	2.90	2.20	2.39	2.65	2.93	1.74	1.78	2.03	2.05	2.65			
$(Eu/Eu^*)_N$	0.45	0.86	0.71	0.84	0.83	0.66	0.69	0.65	0.45	0.80			
Nb/Ta	10.32	14.05	13.64	12.04	12.73	12.63	12.50	13.94	12.65	11.30			
Y/Nb	3.05	4.44	4.73	3.31	4.86	6.79	4.15	6.39	6.09	7.15			
Sr/Y	10.71	11.17	6.06	7.05	10.59	6.00	11.45	5.09	4.16	11.40			
Th/La	0.89	0.33	0.58	0.61	0.37	0.69	0.77	0.47	0.56	0.71			
Ba/Th	99.03	43.24	71.11	10.81	93.33	86.27	81.63	37.50	94.55	82.93			
Th/Yb	3.47	1.39	1.47	2.89	1.65	1.29	1.81	1.44	1.64	3.66			

Rock types	Monzonitic granite						Granodiorite						Dolerite
	BL-055	BL-058	D003	D007	D023	D027	BL-065	D001	D016	D017	D018	D024	BL13-037
SiO_2	68.66	65.68	68.86	70.75	71.35	68.97	67.56	68.63	67.33	69.37	69.56	67.52	45.71
Al_2O_3	13.68	15.49	15.52	15.28	13.63	13.99	15.57	15.17	14.60	14.93	15.00	14.59	16.00
K_2O	1.94	2.51	3.09	3.31	3.21	3.47	1.12	3.18	2.36	2.65	3.27	2.15	0.59
Na_2O	4.05	3.71	3.76	3.00	3.55	3.93	5.00	5.09	4.91	4.81	3.17	3.53	3.96
CaO	2.93	4.09	2.94	3.02	2.70	3.18	4.38	3.43	4.25	3.63	3.21	4.35	3.06
$Fe_2O_3^T$	5.51	4.87	2.51	1.99	2.06	2.26	3.49	1.78	2.61	2.12	2.41	3.05	14.02
MgO	1.02	1.58	1.14	1.03	0.93	1.10	1.55	1.06	1.58	1.25	1.16	1.64	7.86
MnO	0.11	0.05	0.04	0.04	0.05	0.02	0.09	0.09	0.05	0.04	0.04	0.09	0.49
P_2O_5	0.11	0.13	0.10	0.17	0.06	0.09	0.08	0.14	0.08	0.13	0.06	0.10	0.59
TiO_2	0.48	0.50	0.06	0.02	0.32	0.38	0.42	0.02	0.73	0.21	0.40	0.48	2.17
LOI	0.75	1.31	0.96	0.73	0.74	0.97	0.55	0.46	0.73	0.48	0.89	0.52	5.54
Total	99.31	100.00	100.08	100.09	100.12	99.23	99.88	100.09	100.45	100.64	99.98	99.34	100.05
A/CNK	0.97	0.95	1.04	1.09	0.96	0.87	0.89	0.84	0.79	0.86	1.03	0.91	0.87
A/NK	1.56	1.75	1.63	1.79	1.46	1.37	1.65	1.28	1.37	1.38	1.71	1.79	0.80
$Mg^{\#}$	30	43	51	55	51	53	51	58	59	58	53	56	57
Rb	50.10	75.10					25.60						10.60

(continued on next page)

Table 1 (*continued*)

Rock types	Monzonitic granite						Granodiorite						Dolerite
	BL-055	BL-058	D003	D007	D023	D027	BL-065	D001	D016	D017	D018	D024	BL13-037
Ba	450.00	400.00					220.00						80.00
Th	16.30	5.90					8.90						0.70
U	4.80	1.50					1.30						0.50
Nb	5.80	3.60					4.20						11.70
Ta	0.52	0.28					0.40						0.79
La	19.60	8.00					7.90						11.20
Ce	45.30	19.65					16.45						35.10
Pb	6.80	7.50					4.30						115.00
Pr	5.57	2.47					1.81						5.15
Sr	213.00	257.00					347.00						145.50
Nd	22.10	10.60					7.00						24.00
P	480.00	550.00					310.00						2620.00
Sm	4.81	2.61					1.54						6.41
Zr	131.50	23.90					55.60						143.50
Hf	4.00	0.90					1.80						3.50
Eu	1.26	0.79					0.68						1.84
Gd	5.16	2.87					1.77						6.81
Tb	0.83	0.47					0.30						1.07
Dy	5.26	3.05					2.03						6.43
Y	31.40	19.30					14.60						29.40
Ho	1.11	0.66					0.47						1.25
Er	3.23	1.95					1.54						3.47
Tm	0.48	0.29					0.25						0.45
Yb	3.11	1.86					1.72						2.92
Lu	0.51	0.29					0.30						0.43
Co	16.80	10.30					22.00						46.10
Ni	4.20	5.10					6.30						76.70
Cr	42.00	34.00					46.00						72.00
$(La/Yb)_N$	4.52	3.09					3.29						2.75
$(Tb/Yb)_N$	1.21	1.15					0.79						1.67
$(La/Sm)_N$	2.63	1.98					3.31						1.13
$(Eu/Eu^*)_N$	0.77	0.88					1.26						0.85
Nb/Ta	11.15	12.86					10.50						14.81
Y/Nb	5.41	5.36					3.48						2.51
Sr/Y	6.78	13.32					23.77						4.95
Th/La	0.83	0.74					1.13						0.89
Ba/Th	27.61	67.80					24.72						114.29
Th/Yb	5.24	3.17					5.17						0.24

Notes:
The dates abbreviate with "D" from Sang et al. (2003).

into the calc-alkaline and high-K calc-alkaline fields. Most of our studied rocks are metaluminous, with aluminum saturation indices ($[Al_2O_3/(Na_2O + K_2O + CaO)]$) ranging from 0.79 − 1.16 (Fig. 7c). The tuffaceous dacite samples have a wide range of $Mg^{\#}$ values (6–64), whereas the granodiorite, monzonitic granite, and granite range from 30–56, 30–55, and 51–59, respectively. On the Fig. 7d, the Bailingshan granitoids exhibit negative P_2O_5 vs. SiO_2 correlations.

All the studied rocks at Bailingshan display consistent REE patterns, characterized by a LREE enrichment and a flat HREE pattern ($(La/Yb)_N$ = 1.35–4.52; $(Tb/Yb)_N$ = 0.65–1.21; Table 1). Except for one granodiorite sample, the other samples exhibit weak negative Eu anomalies (average Eu/Eu^* = 0.76) (Fig. 8a; Table 1). On the primitive mantle-normalized multi-element plot (Fig. 8b; Sun and McDonough, 1989), geochemistry of all felsic-intermediate rock samples mimics that of arc-related magmas (Pearce and Peate, 1995; Villagómez et al., 2011), with large-ion lithophile element (LILEs; e.g., Rb, K and Pb) enrichment and high field strength element (HFSEs; e.g., Nb, Ta, and Ti) depletion. The studied rocks have relatively low Sr and Sr/Y ratios (average = 9.81), elevated Th, moderate Th/Yb ratios (1.3–3.5), and low Ba/Th ratios (<170) (Table 1).

5.2. Zircon U–Pb ages and Hf isotope

Four samples, including one tuffaceous dacite (BL-004), one granodiorite (BL-065), one monzonitic granite (BL-058), and one granite (BL-050), were dated by zircon U–Pb analysis. The analyzed zircons have a wide range of U and Th contents, and all exhibit high Th/U ratios (>0.4). Their REE patterns are typically characterized by HREE enrichment with positive Ce anomalies and negative Eu anomalies (Fig. 9). Zircon grains are colorless, generally euhedral, and predominantly prismatic, which imply a magmatic origin (Belousova et al., 2002; Li, 2009; Yang et al., 2014).

Eighteen zircons from the dacite (BL-004) yielded $^{206}Pb/^{238}U$ ages ranging from 333–316 Ma, with a weighted mean age of 324.1 ± 2.1 Ma (MSWD = 0.80) (Fig. 10a; Table 2), whereas 20 zircons from the granodiorite (BL-065) yielded $^{206}Pb/^{238}U$ ages ranging from 325–311 Ma, with a weighted mean age of 317.7 ± 1.8 Ma (MSWD = 0.86) (Fig. 10b). The weighted mean $^{206}Pb/^{238}U$ ages of the monzonitic granite (BL-058) and granite (BL-058) are 313.7 ± 2.1 Ma (MSWD = 0.76, n = 21) and 307.2 ± 2.3 Ma (MSWD = 0.70, n = 19), respectively (Fig. 10c–d).

Zircon Hf analyses were performed on the same grains as were used for U–Pb dating. Ten analyses were carried out for each sample. The dacite, granodiorite, monzonitic granite, and granite yielded $\varepsilon_{Hf}(t)$ values (and two-stage Hf model ages) of 3.2–7.5 (1130–888 Ma), 3.3–7.5 (1120–846 Ma), 10.9–13.5 (625–462 Ma), and 10.2–14.4 (675–400 Ma), respectively. For each sample, the $^{176}Lu/^{177}Hf$ ratios are mostly below 0.002 (Table 2), which means that time-integrated changes to the $^{176}Hf/^{177}Hf$ ratio as a result of in-situ decay of ^{176}Lu proceeded at virtually negligible rates (F.Y. Wu et al., 2006). This suggests that the zircons analyzed have preserved the initial $^{176}Hf/^{177}Hf$ ratio of their source area, and can be used to determine the Hf isotopic composition of the source at the time of crystallization.

Table 2
LA-ICP-MS zircon U–Pb age and in-situ Hf isotope analysis data from the Bailingshan area.

	Th/U	$^{207}Pb/^{206}Pb$	±σ	$^{207}Pb/^{235}U$	±σ	$^{206}Pb/^{238}U$	±σ	$^{206}Pb/^{238}U$	$^{176}Lu/^{177}Hf$	$^{176}Hf/^{177}Hf$	±2σ	$\varepsilon_{Hf}(t)$	T_{DM1}	T_{DM2}
BL-004 tuffaceous dacite														
BL-004-1	0.53	0.0568	0.0034	0.3959	0.0235	0.0513	0.0008	322.7	0.000887	0.282672	0.000011	3.4	819	1119
BL-004-2	0.61	0.0533	0.0026	0.3772	0.0185	0.0514	0.0007	322.9	0.001055	0.282730	0.000012	5.4	741	990
BL-004-3	0.68	0.0587	0.0035	0.4069	0.0240	0.0505	0.0008	317.4	0.001371	0.282720	0.000011	4.9	761	1020
BL-004-6	0.61	0.0574	0.0035	0.4026	0.0227	0.0517	0.0009	325.2	0.001134	0.282789	0.000011	7.5	658	855
BL-004-7	0.57	0.0553	0.0029	0.3887	0.0196	0.0512	0.0008	321.7						
BL-004-9	0.59	0.0564	0.0031	0.4107	0.0215	0.0530	0.0008	332.9	0.001042	0.282744	0.000011	6.1	721	952
BL-004-10	0.86	0.0532	0.0025	0.3858	0.0175	0.0523	0.0007	328.4	0.002173	0.282689	0.000011	3.8	824	1095
BL-004-11	0.58	0.0500	0.0024	0.3652	0.0176	0.0523	0.0008	328.6	0.001226	0.282774	0.000011	7.0	681	889
BL-004-13	0.47	0.0581	0.0032	0.4078	0.0224	0.0503	0.0008	316.2						
BL-004-15	0.54	0.0521	0.0029	0.3691	0.0211	0.0515	0.0008	323.5	0.001258	0.282760	0.000011	6.4	702	924
BL-004-16	0.57	0.0528	0.0034	0.3711	0.0220	0.0513	0.0007	322.4	0.001043	0.282682	0.000016	3.7	808	1098
BL-004-17	0.60	0.0532	0.0030	0.3775	0.0205	0.0513	0.0007	322.4	0.001528	0.282671	0.000013	3.2	835	1130
BL-004-18	0.55	0.0536	0.0027	0.3790	0.0182	0.0520	0.0008	326.8						
BL-004-19	0.65	0.0561	0.0029	0.4054	0.0208	0.0525	0.0008	330.0						
BL-004-21	0.63	0.0535	0.0028	0.3828	0.0193	0.0514	0.0006	323.0						
BL-004-22	0.59	0.0546	0.0035	0.3852	0.0244	0.0509	0.0008	320.1						
BL-004-23	0.75	0.0550	0.0030	0.3972	0.0208	0.0519	0.0007	326.5						
BL-004-24	0.55	0.0473	0.0028	0.3322	0.0189	0.0512	0.0007	321.7						
BL-065 granodiorite														
BL-065-1	0.72	0.0553	0.0027	0.3832	0.0190	0.0502	0.0007	315.8						
BL-065-2	0.87	0.0533	0.0025	0.3739	0.0175	0.0510	0.0006	320.4	0.001867	0.282774	0.000010	6.7	693	902
BL-065-5	0.83	0.0550	0.0028	0.3780	0.0196	0.0495	0.0008	311.5	0.001259	0.282798	0.000010	7.5	648	846
BL-065-6	0.63	0.0507	0.0026	0.3595	0.0187	0.0511	0.0007	321.3	0.002038	0.282768	0.000011	6.5	705	918
BL-065-8	0.81	0.0531	0.0019	0.3684	0.0128	0.0501	0.0006	315.4						
BL-065-9	0.74	0.0498	0.0019	0.3536	0.0142	0.0513	0.0008	322.3	0.001748	0.282759	0.000012	6.2	713	935
BL-065-10	0.81	0.0541	0.0026	0.3772	0.0187	0.0502	0.0007	315.9	0.001939	0.282762	0.000012	6.2	711	932
BL-065-11	0.62	0.0523	0.0022	0.3643	0.0155	0.0503	0.0006	316.6						
BL-065-12	1.04	0.0534	0.0022	0.3779	0.0152	0.0513	0.0006	322.4						
BL-065-13	0.70	0.0517	0.0026	0.3681	0.0192	0.0515	0.0008	323.7	0.001555	0.282718	0.000015	4.9	768	1023
BL-065-14	0.66	0.0531	0.0026	0.3697	0.0187	0.0498	0.0006	313.4	0.001501	0.282707	0.000013	4.3	782	1053
BL-065-15	0.75	0.0498	0.0020	0.3459	0.0137	0.0501	0.0005	315.4	0.002241	0.282681	0.000013	3.3	836	1120
BL-065-16	0.61	0.0534	0.0026	0.3719	0.0176	0.0506	0.0007	318.1	0.002192	0.282773	0.000012	6.6	701	910
BL-065-17	1.26	0.0530	0.0022	0.3587	0.0144	0.0494	0.0007	310.5						
BL-065-18	0.68	0.0542	0.0021	0.3791	0.0148	0.0505	0.0006	317.4	0.001646	0.282769	0.000012	6.5	697	913
BL-065-19	0.66	0.0541	0.0021	0.3789	0.0159	0.0498	0.0008	313.4						
BL-065-20	0.75	0.0529	0.0033	0.3742	0.0214	0.0517	0.0007	324.7						
BL-065-21	0.88	0.0497	0.0026	0.3472	0.0177	0.0505	0.0007	317.5						
BL-065-22	0.89	0.0533	0.0023	0.3777	0.0163	0.0508	0.0006	319.4						
BL-065-24	0.97	0.0524	0.0022	0.3732	0.0160	0.0508	0.0006	319.6						
BL-058 monzonitic granite														
BL-058-1	0.72	0.0506	0.0036	0.3377	0.0225	0.0486	0.0007	306.1	0.001329	0.282964	0.000011	13.3	412	474
BL-058-2	0.63	0.0544	0.0029	0.3775	0.0203	0.0493	0.0007	310.4	0.001483	0.282897	0.000009	10.9	510	626
BL-058-3	0.58	0.0560	0.0033	0.3930	0.0220	0.0506	0.0007	318.3						
BL-058-4	0.67	0.0480	0.0028	0.3253	0.0180	0.0489	0.0008	307.6						
BL-058-6	0.65	0.0520	0.0032	0.3633	0.0215	0.0505	0.0007	317.5	0.001110	0.282936	0.000010	12.5	450	528
BL-058-7	0.71	0.0533	0.0030	0.3572	0.0196	0.0489	0.0007	307.6	0.001237	0.282945	0.000009	12.6	438	514
BL-058-8	0.62	0.0525	0.0035	0.3633	0.0240	0.0505	0.0008	317.3	0.000764	0.282938	0.000008	12.7	442	517
BL-058-9	0.58	0.0560	0.0035	0.3747	0.0228	0.0492	0.0008	309.5						
BL-058-10	0.63	0.0558	0.0034	0.3852	0.0243	0.0491	0.0011	309.1						
BL-058-11	0.74	0.0554	0.0041	0.3689	0.0235	0.0504	0.0010	316.8	0.001352	0.282947	0.000009	12.9	437	507
BL-058-12	0.69	0.0540	0.0045	0.3627	0.0266	0.0499	0.0008	313.6	0.001502	0.282968	0.000009	13.5	408	462
BL-058-13	0.42	0.0539	0.0038	0.3598	0.0183	0.0500	0.0008	314.8						
BL-058-14	0.65	0.0517	0.0034	0.3525	0.0223	0.0499	0.0008	314.2	0.001015	0.282946	0.000008	12.8	434	506
BL-058-15	0.64	0.0489	0.0027	0.3429	0.0196	0.0507	0.0008	318.9						
BL-058-16	0.63	0.0480	0.0030	0.3305	0.0198	0.0498	0.0008	313.4	0.001679	0.282943	0.000010	12.6	446	521
BL-058-17	0.60	0.0542	0.0030	0.3716	0.0195	0.0496	0.0008	312.0	0.001372	0.282919	0.000009	11.8	476	571
BL-058-18	0.58	0.0540	0.0026	0.3780	0.0172	0.0508	0.0007	319.4						
BL-058-19	0.64	0.0503	0.0031	0.3410	0.0194	0.0495	0.0008	311.6						
BL-058-21	0.61	0.0552	0.0032	0.3740	0.0204	0.0506	0.0010	318.1						
BL-058-22	0.70	0.0570	0.0033	0.3889	0.0218	0.0500	0.0008	314.3						
BL-058-25	0.56	0.0536	0.0027	0.3746	0.0189	0.0506	0.0007	317.9						
BL-050 granite														
BL-050-1	0.60	0.0492	0.0047	0.3222	0.0291	0.0479	0.0011	301.9	0.001137	0.282996	0.000007	14.3	364	400
BL-050-2	0.52	0.0515	0.0039	0.3596	0.0263	0.0498	0.0011	313.2	0.001228	0.282873	0.000009	10.2	541	675
BL-050-4	0.68	0.0495	0.0030	0.3396	0.0196	0.0495	0.0007	311.7	0.001373	0.282959	0.000009	13.2	419	482
BL-050-6	1.04	0.0502	0.0033	0.3420	0.0209	0.0498	0.0008	313.1						
BL-050-7	0.59	0.0599	0.0047	0.3930	0.0293	0.0485	0.0011	305.2						
BL-050-9	0.51	0.0541	0.0036	0.3639	0.0220	0.0500	0.0009	314.4						
BL-050-10	0.60	0.0522	0.0035	0.3551	0.0233	0.0495	0.0008	311.3	0.001414	0.282993	0.000009	14.4	371	406
BL-050-11	0.80	0.0501	0.0017	0.3410	0.0118	0.0486	0.0006	306.2	0.002948	0.282921	0.000010	11.4	495	592
BL-050-12	0.60	0.0535	0.0041	0.3491	0.0251	0.0485	0.0009	305.4	0.001083	0.282953	0.000010	12.9	425	496

(continued on next page)

Table 2 (*continued*)

	Th/U	$^{207}Pb/^{206}Pb$	±σ	$^{207}Pb/^{235}U$	±σ	$^{206}Pb/^{238}U$	±σ	$^{206}Pb/^{238}U$	$^{176}Lu/^{177}Hf$	$^{176}Hf/^{177}Hf$	±2σ	$\varepsilon_{Hf}(t)$	T_{DM1}	T_{DM2}
BL-050 granite														
BL-050-13	0.54	0.0589	0.0045	0.3903	0.0292	0.0492	0.0010	309.6						
BL-050-14	0.50	0.0593	0.0051	0.3786	0.0292	0.0482	0.0009	303.6						
BL-050-15	0.84	0.0532	0.0034	0.3567	0.0226	0.0483	0.0007	304.1	0.001059	0.282964	0.000009	13.3	409	471
BL-050-17	0.49	0.0580	0.0046	0.3759	0.0275	0.0478	0.0009	300.9						
BL-050-18	0.54	0.0574	0.0050	0.3766	0.0306	0.0496	0.0009	312.2	0.000931	0.282963	0.000009	13.4	409	467
BL-050-19	0.48	0.0548	0.0042	0.3699	0.0273	0.0490	0.0009	308.5	0.001065	0.282971	0.000008	13.6	399	452
BL-050-20	0.62	0.0573	0.0040	0.3824	0.0261	0.0482	0.0009	303.7	0.001470	0.282961	0.000009	13.1	418	484
BL-050-22	0.58	0.0568	0.0042	0.3842	0.0272	0.0490	0.0009	308.6						
BL-050-23	0.58	0.0548	0.0043	0.3614	0.0259	0.0481	0.0008	302.9						
BL-050-25	0.49	0.0513	0.0039	0.3380	0.0254	0.0478	0.0008	300.9						

Notes: $\varepsilon_{Hf}(t) = 1000\{[(^{176}Hf/^{177}Hf)_S - (^{176}Lu/^{177}Hf)S \times (e^{\lambda t} - 1)] / [(^{176}Hf/^{177}Hf)_{CHUR,0} - (^{176}Lu/^{177}Hf)CHUR \times (e^{\lambda t} - 1)] - 1\}$.
$T_{DM1} = 1/\lambda \times \ln\{1 + [(^{176}Hf/^{177}Hf)_S - (^{176}Hf/^{177}Hf)_{DM}] / [((^{176}Lu/^{177}Hf)_S - (^{176}Lu/^{177}Hf)_{DM})]\}$.
$T_{DM2} = 1/\lambda \times \ln\{1 + [(^{176}Hf/^{177}Hf)_{S,t} - (^{176}Hf/^{177}Hf)_{DM,t}] / [((^{176}Lu/^{177}Hf)_c - (^{176}Lu/^{177}Hf)_{DM}]\} + t$.
The $^{176}Hf/^{177}Hf$ and $^{176}Lu/^{177}Hf$ ratios of chondrite and depleted mantle at the present day are 0.282772 and 0.0332, and 0.28325 and 0.0384, respectively (Griffin et al., 2004). $\lambda_{Lu} = 1.867 \times 10^{-11}$ year^{-1} (Soderlund et al., 2004). $(^{176}Lu/^{177}Hf)_C = 0.015$ (Griffin et al., 2002). It is the crystallization age of zircon.

5.3. Whole-rock Sr–Nd–Pb isotopes

Initial isotopic ratios were calculated back to the crystallization age of the studied rocks. The tuffaceous dacite shows low initial $^{87}Sr/^{86}Sr$ ratios (0.70427–0.70530). In terms of Nd isotopic ratios, the studied rocks at Bailingshan are characterized by positive $\varepsilon_{Nd}(t)$ values (2.03–4.41). The corresponding T_{DM} ages of the dacite (single stage depleted mantle model ages; Liew and Hofmann, 1988) vary in a narrow range (T_{DM} = 0.91–1.09 Ga). The T_{DM} ages of the granitoid samples suggest their source is Proterozoic in age. The granodiorite, monzonitic granite, and granite have I_{Sr} ratios (0.70475, 0.70390 and 0.70397, respectively), $\varepsilon_{Nd}(t)$ values (3.90, 5.78, and 5.94, respectively), and T_{DM} ages (0.84, 0.74, and 0.69 Ga, respectively) similar to the dacite (Table 3).

In summary, the studied rocks at Bailingshan are characterized by low $^{87}Sr/^{86}Sr$ and high $^{143}Nd/^{144}Nd$ values, and deviate from the mantle evolution trend in the $\varepsilon_{Nd}(t)$ vs. I_{Sr} diagram (Fig. 11a). In terms of Pb isotopes, all the analyzed felsic-intermediate rock types have low $(^{206}Pb/^{204}Pb)_t$ and $(^{207}Pb/^{204}Pb)_t$ and high $(^{208}Pb/^{204}Pb)_t$ (Table 4). On the $(^{206}Pb/^{204}Pb)_t$ vs. $(^{207}Pb/^{204}Pb)_t$ diagram (Fig. 11b), most samples plot in the ocean island basalt (OIB) field.

6. Discussion

6.1. Ages of the magmatic events at Bailingshan

As mentioned above, analyzed zircons from the Bailingshan tuffaceous dacite, granodiorite, monzonitic granite, and granite have igneous oscillatory zonation, elevated Th/U ratios (0.53–0.75, 0.42–0.74, 0.48–1.04 and 0.53–0.75, respectively), HREE enrichment, positive Ce anomalies, and negative Eu anomalies, which together indicate a magmatic origin (Figs. 9 and 10). Therefore, the U–Pb ages accurately reflect the magmatic ages of the studied Bailingshan rocks (Buick et al., 1995; Yang et al., 2014).

Rocks of the Tugutublak volcanic–sedimentary sequence are exposed on both sides of the Aqikekuduke Fault (Zhang et al., 2012). The presence of indicator fossils, such as corals and fusulinids, within the intercalated bioclastic limestone that is exposed in Lubaishan and Jiabaishan areas in the middle part of the Aqishan–Yamansu arc belt suggested that the rocks of the Tugutublak Formation formed in the Late Carboniferous (Zhang et al., 2012). The youngest formation age was previously constrained by a SHRIMP zircon U–Pb age (314 ± 4.2 Ma) for the granodiorite near Lubaishan that was emplaced into the formation (Song et al., 2006). In this study, our 324 ± 2.1 Ma tuffaceous dacite (BL-004) age represents the first absolute age for the Tugutublak volcanic rocks, and it agrees with the paleontological constraints.

Previous studies suggested that syn-arc and post-arc granitic magmatism of the Aqishan–Yamansu belt occurred from ca. 349 to 228 Ma (Table 5) in three episodes (C.Z. Wu et al., 2006; Zhou et al., 2010; Lei et al., 2013). These included the Carboniferous (ca. 349–303 Ma), Early Permian (ca. 297–272 Ma), and Middle to Late Triassic (ca. 246–228 Ma) stages, with a general eastward younging trend. Geodynamic studies indicate that the late Paleozoic granitoids are arc-related, whereas the Triassic granitoids were emplaced in a post-collisional setting (C.Z. Wu et al., 2006; Zhou et al., 2010; Lei et al., 2013). The Carboniferous granitoids occur mainly in the western part of the Aqishan–Yamansu arc belt, including the Xifengshan, Changtiaoshan, Hongyuntan, and Bailingshan plutons that comprise

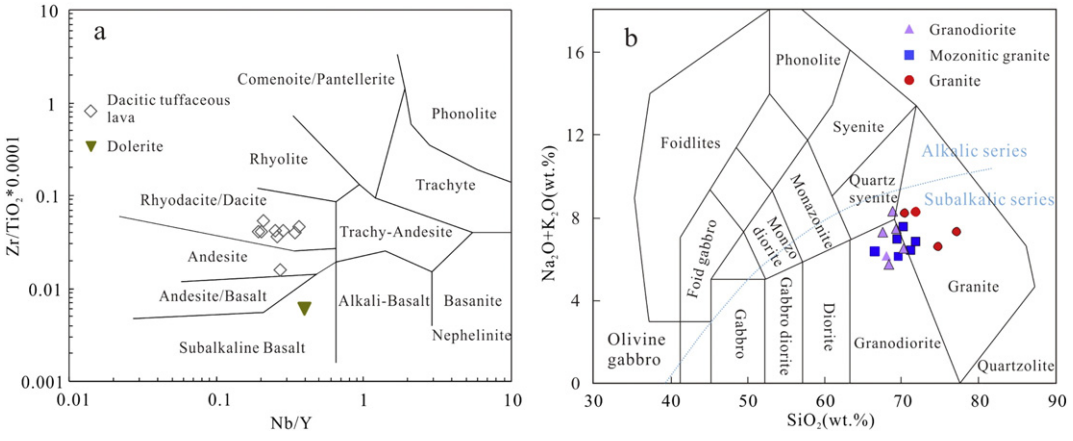

Fig. 6. (a) Zr/TiO_2*0.0001 vs. Nb/Y diagram for the tuffaceous dacitic lava (after Winchester and Floyd, 1976); (b) Total alkalis vs. silica diagram for the Bailingshan granitoids (after Wilson, 1989), data with circle are from Sang et al. (2003).

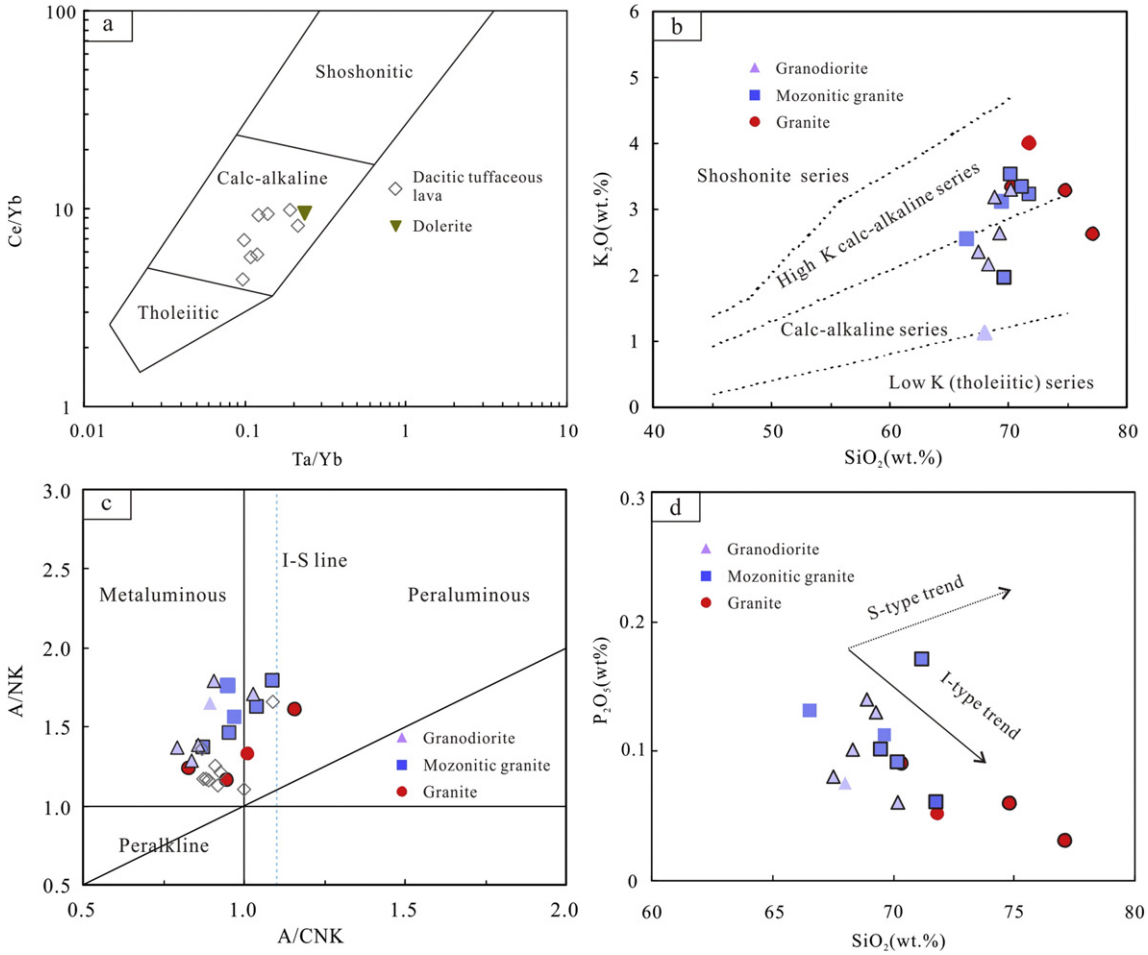

Fig. 7. (a) Ce/Yb vs. Ta/Yb diagram for the tuffaceous dacitic lava (after Müller et al., 1992). (b) K_2O vs. SiO_2 diagram for the Bailingshan granitoids (after Peccerillo and Taylor, 1976). (c) A/NK vs. A/CNK diagram (after Maniar and Piccoli, 1989). (d) P_2O_5 vs. SiO_2 diagram for the Bailingshan granitoids. A/CNK = molar $Al_2O_3/(Na_2O + K_2O + CaO)$, A/NK = molar $Al_2O_3/(Na_2O + K_2O)$.

granite and granodiorite. The Early Permian plutons are mainly distributed in the middle part of the arc belt, represented by the Weiquan, Longdong, and Duotoushan intrusions, which comprise granodiorite, monzonitic granite, and granite, respectively. The Middle to Late Triassic granites are mainly distributed in the eastern part of the belt, e.g., the Tudun and Yamansubei granites.

Zhou et al. (2010) first reported a zircon U–Pb age for the Bailingshan granodiorite of 317.7 ± 3.5 Ma. In this study, we report a similar age for the Bailingshan granodiorite of 317.7 ± 1.8 Ma, but younger ages for the Bailingshan monzonitic granite (313.7 ± 2.1 Ma) and granite (307.2 ± 2.3 Ma). Therefore, the granitic magmatism at Bailingshan may have taken place as soon as a couple of million years after Tugutublak Formation volcanism, and definitely within 10 million years of deposition of the volcanic rocks.

6.2. Timing of Fe mineralization

The Bailingshan Fe deposit is a skarn deposit, yet the spatial relationship between the exoskarn orebodies and causative igneous rocks is still ambiguous. It is clear is that the mineralization is spatially related to a

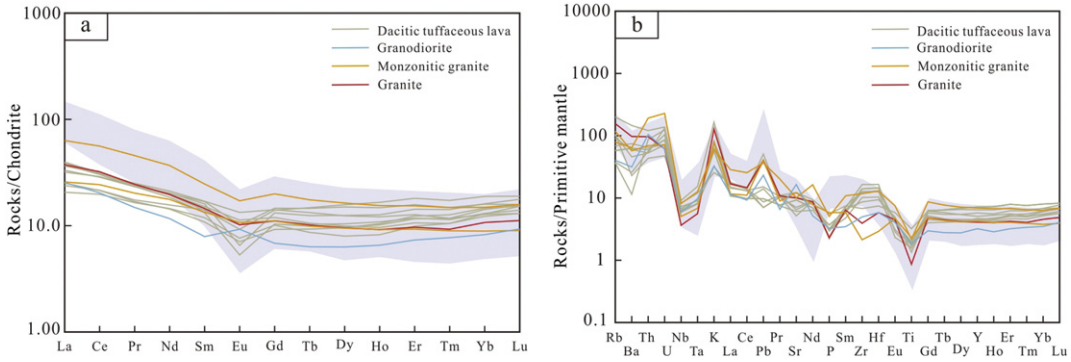

Fig. 8. (a) Chondrite-normalized REE patterns. (b) Primitive mantle-normalized multi-element diagrams. The dashed area represents the compositions range of arc-related coastal batholith in the Central Andean district (Villagómez et al., 2011). Data of average chondrite and primitive mantle are from Boynton (1984) and Sun and McDonough (1989), respectively.

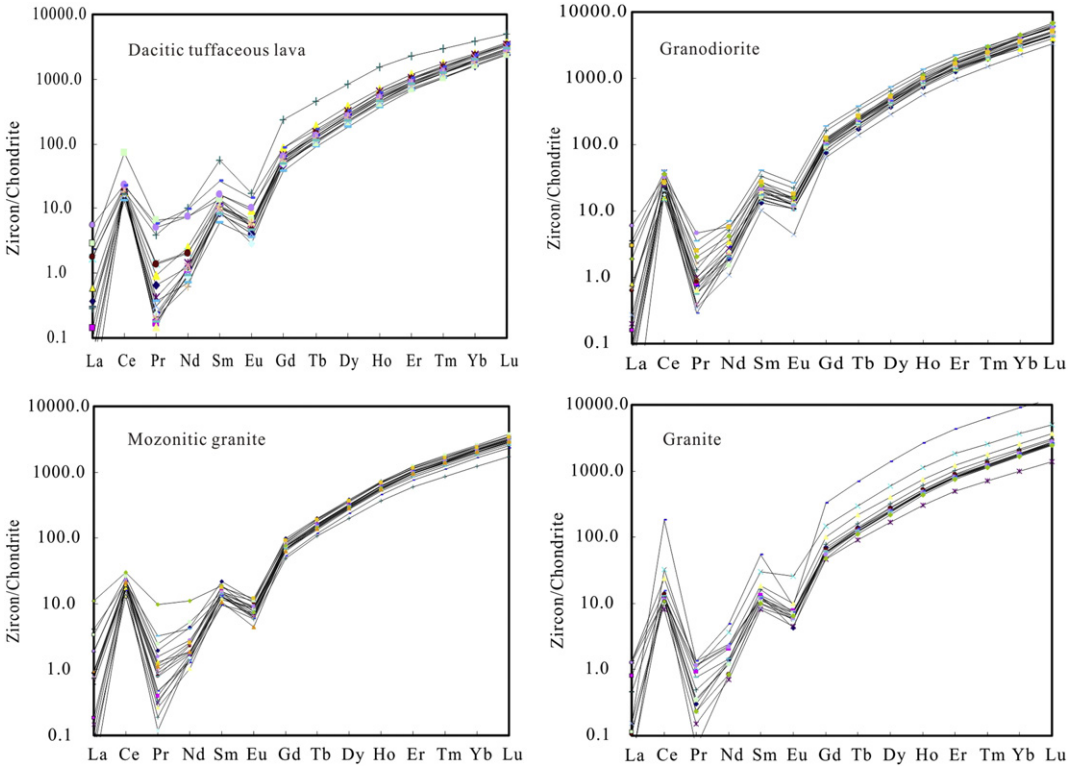

Fig. 9. Chondrite-normalized REE patterns for the igneous zircons from: (a) Tuffaceous dacitic lava (sample BL-004). (b) Granodiorite (sample BL-065). (c) Monzonitic granite (sample BL-058). (d) Granite (sample BL-050).

region with extensive magmatic activity (Meng et al., 2013), and our new field and petrographic evidence support a genetic relationship for a couple of reasons. First, skarn minerals, such as garnet, clinopyroxene, amphiboles, and epidote are well-developed in the deposit (Fig. 4), and these are typically the products of magmatic-hydrothermal activity. Secondly, H–O isotope data for the garnets have shown that the early fluids have a magmatic origin, and some fluid inclusions in garnets homogenized to vapor by liquid disappearance above 600 °C (Weifeng Zhang, unpublished data). Thus mineralization was certainly associated with some phase of Bailingshan granitic magmatism, although direct contact relationships between the intrusions and the orebodies are yet to be seen in outcrops or drill cores. Based on the above geochronological evidence, the ages of the Bailingshan granodiorite (ca. 317.7 Ma) and granite (ca. 307.2 Ma) are interpreted to represent the maximum and the minimum mineralization ages, respectively. This age range for Fe skarn formation is broadly coeval with the published Re–Os ages from the Fe–Cu deposits (e.g., Hengfengshan, 312 ± 23 Ma; Shuangfengshan, 294.5 ± 7.2 Ma; Shaquanzi, 295.2 ± 7.3 Ma) in the Aqishan–Yamansu mineralization belt, which indicates a major Late Carboniferous–Early Permian Fe and Fe–Cu mineralization epoch (Huang et al., 2013).

6.3. Petrogenesis and sources of the Bailingshan magmatism

6.3.1. Tugutublak Formation tuffaceous dacitic lava

The Tugutublak dacite is characterized by pronounced depletion of HFSEs (Nb, Ta, and Ti) and enrichment in LILEs (Rb, K and Pb), which can generally be attributed to either subduction-related metasomatism or intraplate crustal contamination (Pearce and Cann, 1973; McCulloch and Gamble, 1991). However, the lack of inherited zircons in the dacite suggests that crustal contamination only played a minor role in the petrogenesis (De Haller et al., 2006).

As shown in Table 1, the tuffaceous dacite has a high SiO_2 content (average = 71.8 wt.%) and relatively low contents of compatible trace elements, such as Ni, Cr, and Co (Table 1), suggesting a possible crustal source. Jahn and Zhang (1984) reported that felsic rocks with a high SiO_2 content (>66%) couldn't be generated directly by the partial melting of mantle peridotite. Green (1995) suggested that Nb and Ta have similar geochemical properties, with the average Nb/Ta values for mantle- and crustal-derived magmas being 17.5 and 11–12, respectively. The Nb/Ta values for the Tugutublak dacite range from 10.3–14.1 (average = 12.72, Fig. 12), overlapping the range for crustal-derived magmas. In addition, elevated Y/Nb values of the tuffaceous dacite (3.14–6.79) (Table 2) also point to a crustal (Y/Nb > 2) origin (Eby, 1992). The in-situ Hf isotopic analysis of zircons, combined with their U–Pb ages, provides a robust method to trace the source and petrogenesis of magmas, and to constrain the crustal evolution history (Woodhead et al., 2001; Kinny and Maas, 2003; F.Y. Wu et al., 2006; Kemp et al., 2007; Santosh et al., 2015). Kinny and Maas (2003) have shown that negative $\varepsilon_{Hf}(t)$ values indicate source materials derived from partial melting of older crust and positive $\varepsilon_{Hf}(t)$ values indicate derivation from juvenile magmas. The zircon Hf isotope model ages represent the extraction time of source materials from the depleted mantle and the residence time in the crust (Griffin et al., 2002). The Tugutublak tuffaceous dacite has positive $\varepsilon_{Hf}(t)$ values varying from +3.2 to +7.5, with the corresponding Hf depleted model ages (T_{DM}) ranging from 1130 Ma to 888 Ma. These data indicate that the Tugutublak magma was likely derived from a juvenile basaltic lower crust, as is also supported by low initial $^{87}Sr/^{86}Sr$ (0.70427 to 0.70530), $(^{206}Pb/^{204}Pb)_t$ (17.05 to 17.84), and $(^{207}Pb/^{204}Pb)_t$ (15.48 to 15.52), and positive $\varepsilon_{Nd}(t)$ (+2.03 to +4.41) (Fig. 11). Previous studies indicate that the juvenile crustal components in arc systems can be sourced either from crustal underplating during back-arc extension (McKenzie, 1989; Vervoort and Blichert-Toft, 1999; Mišković and Schaltegger, 2009) or from melting of a subducted oceanic slab (Zhang et al., 2006; Richards and Kerrich, 2007; Hou et al., 2013). However, significant slab melting is precluded by the low Sr/Y and $(La/Yb)_N$ values (Table 1). As shown in Fig. 13a, all of the samples plot outside the adakite field and inside the normal arc field. Consequently, underplated juvenile lower

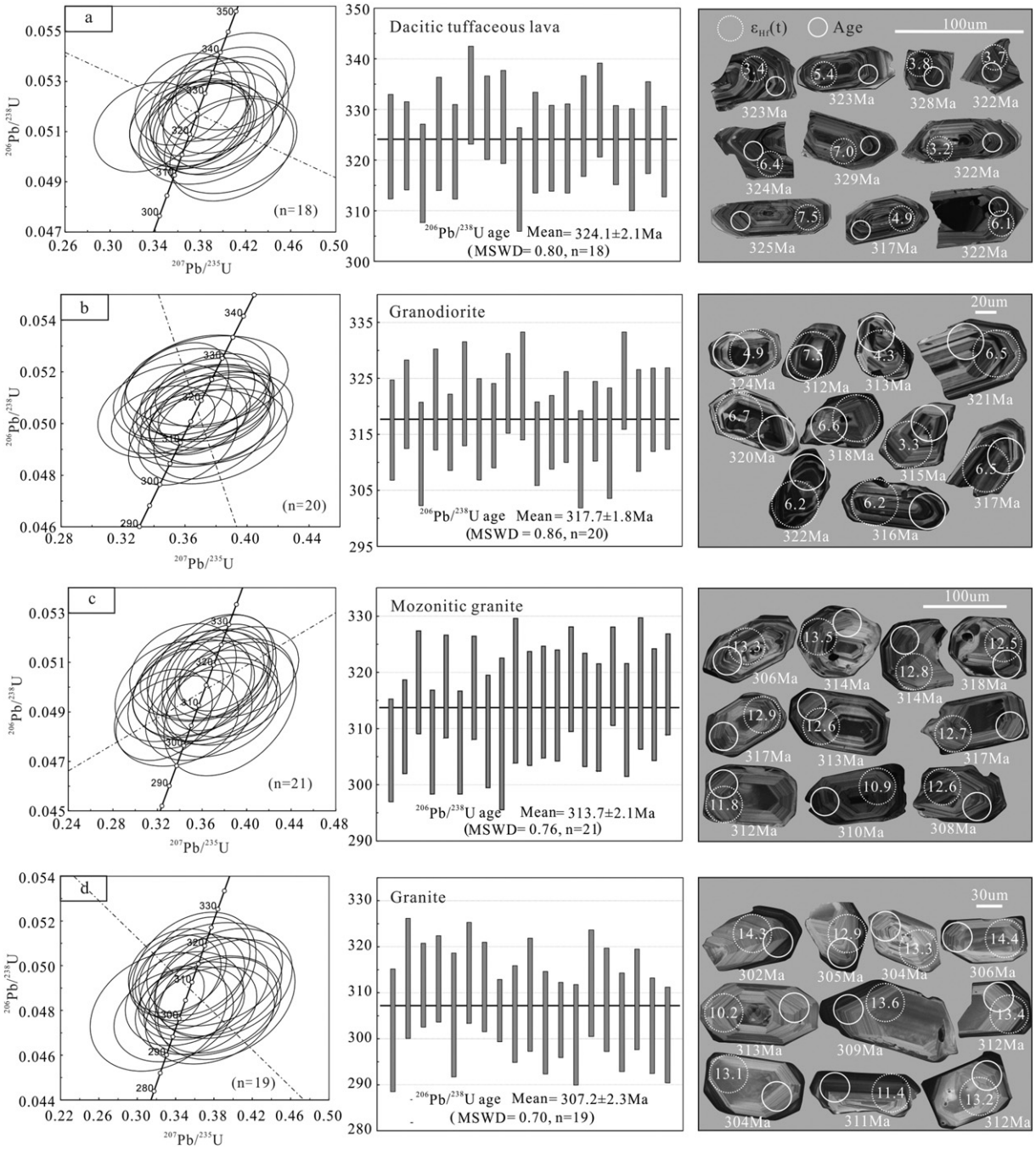

Fig. 10. Concordia diagrams, CL images and in-situ Hf isotopes of the zircons from: (a) Tuffaceous dacitic lava (sample BL-004). (b) Granodiorite (sample BL-065). (c) Monzonitic granite (sample BL-058). (d) Granite (sample BL-050).

Table 3
Sr and Nd isotope compositions of samples from the Bailingshan area.

Sample	Type	Age (Ma)	Rb (ppm)	Sr (ppm)	$^{87}Rb/^{86}Sr$	$^{87}Sr/^{86}Sr$	2σ	I_{Sr}	Nd (ppm)	Sm (ppm)	$^{147}Sm/^{144}Nd$	$^{143}Nd/^{144}Nd$	2σ	$f_{Sm/Nd}$	T_{DM}(Ga)	$\varepsilon_{Nd}(t)$
BL-004	Dacitic tufflava	324.1	127.00	212.00	1.71031	0.71312	8	0.70523	11.10	2.58	0.1405	0.512628	5	−0.29	1.09	2.14
BL-008	Dacitic tufflava	324.1	67.20	258.00	0.74363	0.70873	7	0.70530	12.70	3.31	0.1576	0.512659	6	−0.20	1.33	2.03
BL-009	Dacitic tufflava	324.1	64.90	129.00	1.43635	0.71090	7	0.70427	8.60	2.11	0.1483	0.512761	6	−0.25	0.91	4.41
BL-065	Granodiorite	317.7	25.60	347.00	0.21063	0.70571	8	0.70475	7.00	1.54	0.1330	0.512705	5	−0.32	0.84	3.90
BL-058	Monzonitic granite	313.7	75.10	257.00	0.83428	0.70763	7	0.70390	10.60	2.61	0.1488	0.512836	5	−0.24	0.74	5.78
BL-050	Granite	307.2	99.40	212.00	1.33862	0.70982	7	0.70397	11.80	2.83	0.1450	0.512838	5	−0.26	0.69	5.94

The isotopic ratios measured are normalized to $^{87}Sr/^{86}Sr = 0.1194$ and $^{146}Nd/^{144}Nd = 0.7219$. Initial $^{87}Sr/^{86}Sr$ ratios are calculated using $\lambda_{Rb} = 1.42 \times 10^{-11}$ (Steiger and Jäger, 1977). Initial $^{143}Nd/^{144}Nd$ ratios and $\varepsilon_{Nd}(t)$ are calculated using $\lambda_{Sm} = 6.54 \times 10^{-12}$ (Lugmair and Harti, 1978) and present-day Bulk Earth values are $^{147}Sm/^{144}Nd = 0.1967$, $^{143}Nd/^{144}Nd = 0.512638$.

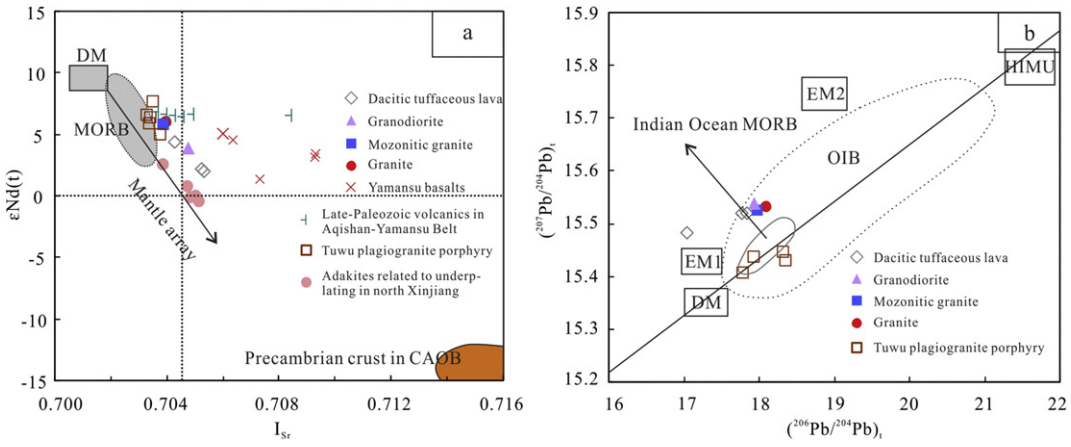

Fig. 11. (a) $\varepsilon_{Nd}(t)$ vs. I_{Sr} diagram for the tuffaceous dacitic lava and Bailingshan granitoids. All data were calculated to the corresponding zircon U–Pb ages. Data for the Yamansu basalts from Hou et al. (2014); Data for the late Paleozoic volcanics in the Aqishan–Yamansu belt from Muhetaer et al. (2014); data for the Tuwu plagiogranite porphyries from Zhang et al. (2006); data for the adakites related to underplating in northern Xingjiang from Zhao et al. (2008). The field of the Precambrian CAOB crust after Chen et al. (2013). (b) Lead isotopic geotectonic framework diagram after Zhou and Mukasa (1997).

crustal components are assumed to be the source for the Tugutublak dacitic magma.

Experimental studies demonstrate that the $Mg^{\#}$ is a useful index to discriminate melts derived solely from the crust from those with mantle involvement. Generally, melts from the basaltic lower crust are characterized by a low $Mg^{\#}$ (<40), regardless of the degree of melting, whereas those with a $Mg^{\#} > 40$ can only be formed when a mantle component is involved (Rapp and Watson, 1995; Smithies and Champion, 2000). In this study, some of the tuffaceous dacite samples have relatively low MgO contents and $Mg^{\#}$ values, ranging from 0.12 to 0.73 wt.% and from 6 to 31, respectively, which resembles melts derived from a basaltic lower crust. However, other samples have higher MgO and $Mg^{\#}$ values (41–64), and suggest an involvement of mantle-derived materials. Together with the relatively wide range (up to +7.5 ε units) for zircon $\varepsilon_{Hf}(t)$ and Nb/Ta (10.3–14.1) measured for the Tugutublak tuffaceous dacite (Table 3), it is inferred that mantle-derived melts were involved in the generation of the Late Carboniferous host rocks for the intrusions and skarns. This conclusion agrees with previously published geochemical data from the eastern Tianshan (Muhetaer et al., 2014), which also suggest that the Late Carboniferous magmatic suite in the Aqishan–Yamansu arc belt was derived from a crustal–mantle mixed source.

Taking all the above evidence into account, we conclude that the Tugutublak tuffaceous dacite was probably derived from the melting of a juvenile basaltic lower crust that mixed with mantle-derived material.

6.3.2. The Bailingshan granitoids

Although granites can be generally subdivided into I-, S-, and A-type according to their protoliths (Pitcher, 1993), distinction between different granite types is not always straightforward, particularly between A-type and highly fractionated I-type (Whalen et al., 1987; Chappell and White, 1992). Although the major element contents of many A-type granites resemble those of the fractionated I-types, A-type granites contain higher total FeO, MnO, Na_2O, Zr, Nb, Y, La, Ce, Sc, Zn, and Ga than both I- and S-type granites (Chappell and White, 1992). The Bailingshan granitoids contain low Zr, Nb, Y, Ce, and FeO^T/MgO (1.8–5.5), and do

Table 4
Pb isotope composition of samples from the Bailingshan area.

Sample	Type	Age (Ma)	Pb (ppm)	Th (ppm)	U (ppm)	$^{206}Pb/^{204}Pb$	$(^{206}Pb/^{204}Pb)_t$	$^{207}Pb/^{204}Pb$	$(^{207}Pb/^{204}Pb)_t$	$^{208}Pb/^{204}Pb$	$(^{208}Pb/^{204}Pb)_t$
BL-004	Dacitic tufflava	324.1	9.4	10.3	2.9	18.93	17.76	15.58	15.52	38.94	37.62
BL-008	Dacitic tufflava	324.1	7.0	3.7	1.0	18.38	17.84	15.55	15.52	38.40	37.77
BL-009	Dacitic tufflava	324.1	2.6	4.5	1.5	19.26	17.05	15.60	15.48	39.22	37.12
BL-065	Granodiorite	317.7	4.3	8.9	1.3	19.05	17.94	15.60	15.54	40.07	37.67
BL-058	Monzonitic granite	313.7	7.5	5.9	1.5	18.72	17.99	15.56	15.53	38.72	37.81
BL-050	Granite	307.2	7.5	8.2	1.3	18.75	18.10	15.57	15.53	38.76	37.48

Table 5
Summary of geochronological data for granitoids in the Aqishan-Yamansu Belt, Eastern Tianshan.

Location	Date rocks	Dating method	Ages/Ma	Date sources
Xifengshan	Granite	LA-ICP-MS zircon U–Pb	349 ± 3.4	Zhou et al. (2010)
Changtiaoshan	Quartz diorite porphyrite	LA-ICP-MS zircon U–Pb	337.4 ± 2.8	Zhou et al. (2010)
Hongyuntan	Granodiorite	LA-ICP-MS zircon U–Pb	328.5 ± 9.3	C.Z. Wu et al. (2006)
Bailingshan	Granodiorite	LA-ICP-MS zircon U–Pb	317.7 ± 3.7	Zhou et al. (2010)
	Granodiorite	LA-ICP-MS zircon U–Pb	317.7 ± 1.8	This study
	Monzonitic granite	LA-ICP-MS zircon U–Pb	313.7 ± 2.1	This study
	Granite	LA-ICP-MS zircon U–Pb	307.2 ± 2.3	This study
Weiquan	Granodiorite	SHRIMP zircon U–Pb	297 ± 3	Wang et al. (2005)
Longdong	Monzonitic granite	LA-ICP-MS zircon U–Pb	276.2 ± 2.5	Zhou et al. (2010)
Duotoushan	Granite	LA-ICP-MS zircon U–Pb	271.7 ± 5.5	Zhou et al. (2010)
Tudun	Granite	LA-ICP-MS zircon U–Pb	246.2 ± 2.6	Zhou et al. (2010)
Yamansubei	Granite	LA-ICP-MS zircon U–Pb	227.9 ± 0.47	Lei et al. (2013)

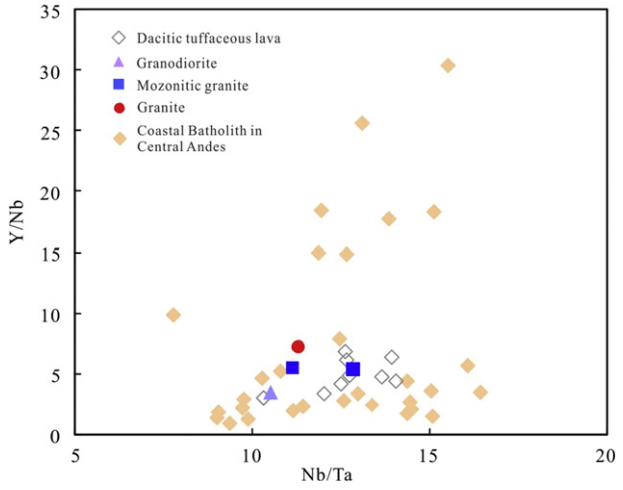

Fig. 12. Nd/Ta vs. Y/Nd diagram. Data of Coastal Batholith in Central Andes from Cochrane et al. (2014).

not fall into the A-type field in the $(K_2O + Na_2O)/CaO$ vs. $(Zr + Nb + Ce + Y)$ diagrams (Fig. 13b; Whalen et al., 1987).

In terms of I- and S-type granite classification, Chappell and White (1974) used A/CNK (aluminum saturation index: molecular $Al_2O_3/(Na_2O + K_2O + CaO)$) ≫ 1.1 to distinguish S-type granites from I-type ones. This differentiation does not always work, particularly when A/CNK values overlap in highly fractionated I- and S-type granites (Chappell, 1999; Wu et al., 2003). The granite, monzonitic granite, and granodiorite at Bailingshan are metaluminous, with A/CNK ranging from 0.83–1.16 (Fig. 7c, Table 1). When granites fractionate, P_2O_5 increases in peraluminous S-type melts, but decreases in I-type melts (Chappell, 1999; Wu et al., 2003). As shown in Fig. 7d, P_2O_5 decreases with increasing SiO_2 for the Bailingshan granitoids, and thus the rocks are best classified as I-type. Han and Ma (2003) pointed out that the I_{Sr} value could also be used to distinguish I-type ($I_{Sr} < 0.707$) from S-type ($I_{Sr} > 0.707$) granites. The I_{Sr} values of the studied granitoids range from 0.7039–0.7045, which are consistent with the I-type classification. Moreover, S-type granites contain Al-rich biotite and other Al-rich minerals, whereas I-type granites contain mainly hornblende; S-type granites commonly contain ilmenite rather than magnetite, whereas I-type granites contain mainly magnetite, although ilmenite-bearing varieties are also present (Chappell, 1999). Petrographic analyses show that the Bailingshan granitoids contain hornblende (Fig. 5d, f, h) and magnetite, but lack cordierite, garnet, monazite, and ilmenite, suggesting the rocks are I-type.

Calc-alkaline to high-K calc-alkaline I-type granitoids can be generated via (1) partial melting of mafic to intermediate (meta)-igneous rocks without sediment involvement (Chappell and White, 2001) or by (2) mingling of juvenile crustal-derived and mantle-derived magmas (Kemp et al., 2007). Studies indicate that Hf isotopic compositions in zircons are useful in determining possible magma sources (e.g., Woodhead et al., 2001; F.Y. Wu et al., 2006; Kemp et al., 2007). The Bailingshan granitoid samples have Nb/Ta ratios of 10.50–12.86 and low contents of Ni, Cr, and Co, indicating a crustal source (11–12; Green, 1995). In addition, the samples have very low Sr concentrations (212–347 ppm) and Sr/Y ratios (6.78–23.77), which are markedly different from typical adakitic rocks, but comparable to normal arc rocks (Whalen et al., 1987; Fig. 13a). The Bailingshan granitoids furthermore show isotopically juvenile component characteristics, such as positive zircon $\varepsilon_{Hf}(t)$ values (granodiorite: 3.3–7.5; monzonitic granite: 10.9–13.5; granite: 10.2–14.4) and positive $\varepsilon_{Nd}(t)$ (3.90, 5.78, and 5.94, respectively) (Tables 2 and 3), suggesting the juvenile crustal rocks may have formed during crustal underplating. Meanwhile, the granitoids at Bailingshan have relatively high $Mg^{\#}$ (granodiorite: 51–59; monzonitic granite: 30–55; granite: 30–56), implying an involvement of mantle-derived materials. In conclusion, mingling of juvenile crust-derived magmas and mantle-derived magmas can account for the formation of the Bailingshan granitoids.

Compared to dacite, the Bailingshan granitoids exhibit elevated zircons $\varepsilon_{Hf}(t)$ values and $\varepsilon_{Nd}(t)$ (Tables 2 and 3; Fig. 14a–b), indicating that the mantle component may have played a more prominent role in the formation of the Bailingshan granodiorite, and even more so for the younger granite and monzonitic granite.

6.4. Implications for tectonic setting

Although the tectonic history of the Aqishan–Yamansu arc belt has been widely discussed (W.M. Li et al., 2002; Xiao et al., 2004; Li et al., 2006; Hou et al., 2014; Wang et al., 2014), its late Paleozoic tectonic setting is still controversial. Major controversies lie in the subduction polarity and the existence of a back (intra)-arc basin. Xiao et al. (2004) suggested that the Aqishan–Yamansu belt was formed as a result of a north-dipping subduction of the South Tianshan oceanic plate, which lasted from the Devonian to the Late Carboniferous. Hou et al. (2014) suggested that a south-dipping subduction of the Junggar oceanic plate had formed the Dananhu–Tousuquan island arc–Aqishan–Yamansu back-arc basin system. A third hypothesis proposed that a bipolar subduction of the Kanggur oceanic plate had generated the

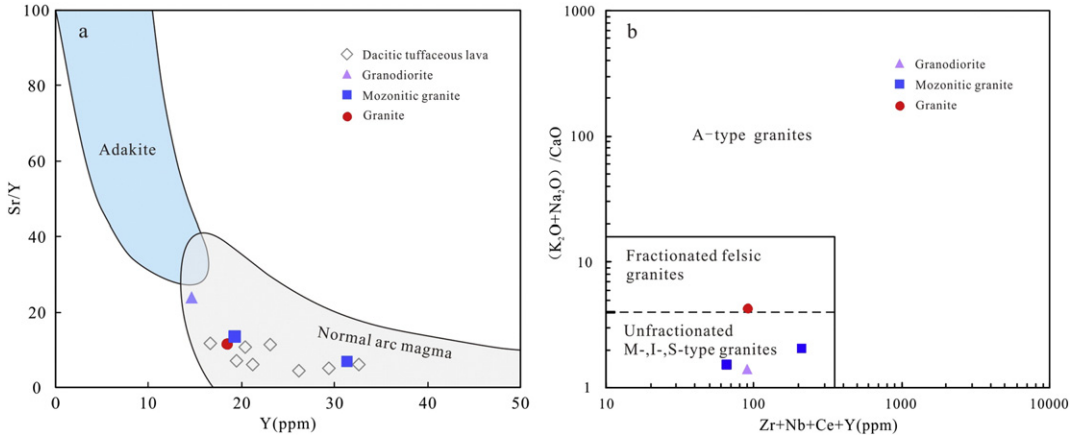

Fig. 13. (a) Sr/Y vs. Y diagram (modified after Defant and Drummond, 1990). (b) $(K_2O + Na_2O)/CaO$ vs. $(Zr + Nb + Ce + Y)$ diagram for the Bailingshan granitoids. Diagram modified from Whalen et al. (1987).

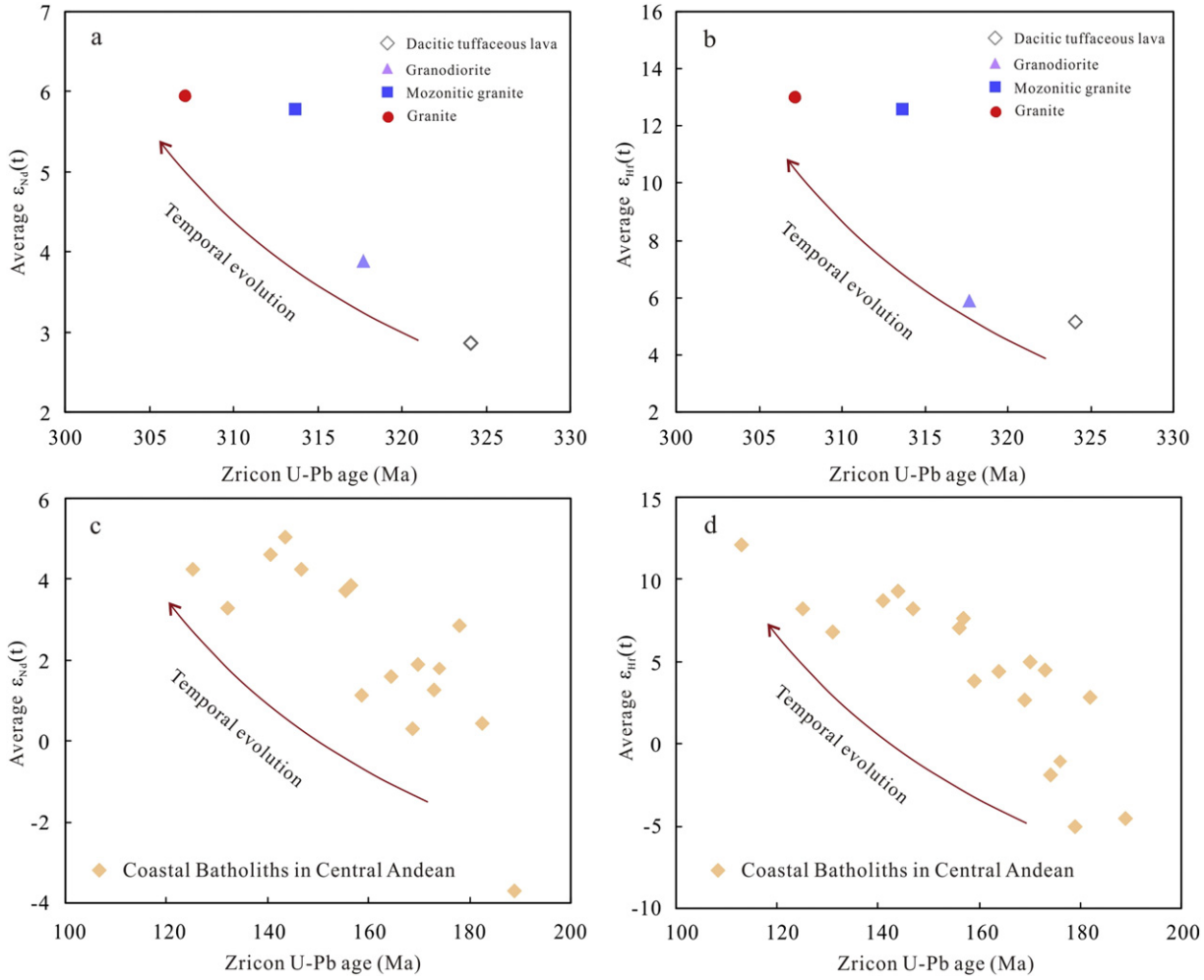

Fig. 14. (a) Average $\varepsilon_{Nd}(t)$ vs. zircon U–Pb age diagram for the tuffaceous dacitic lava and Bailingshan granitoids. (b) Average $\varepsilon_{Hf}(t)$ vs. zircon U–Pb age diagram for the tuffaceous dacitic lava and Bailingshan granitoids. (c) Average $\varepsilon_{Nd}(t)$ vs. zircon U–Pb age diagram for the Coastal Batholith in Central Andes (Cochrane et al., 2014). (d) Average $\varepsilon_{Hf}(t)$ vs. zircon U–Pb age diagram for the Coastal Batholith in Central Andes (Cochrane et al., 2014).

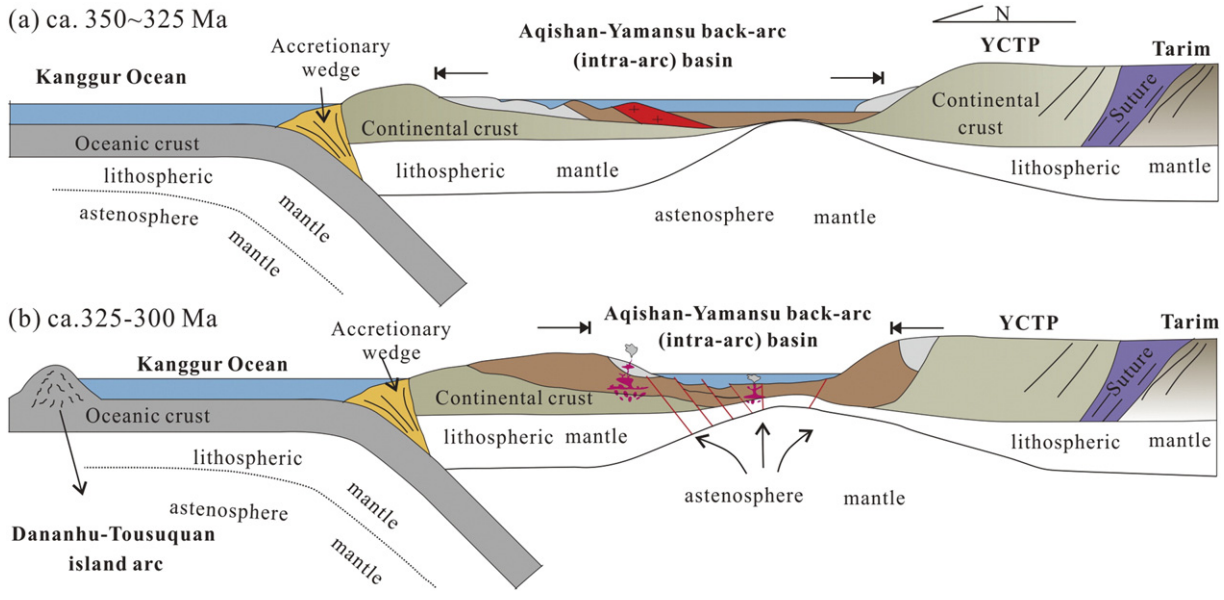

Fig. 15. Schematic geodynamic model of the Aqishan–Yamansu belt during the late Carboniferous.

Aqishan–Yamansu island arc in the south and the Dananhu–Tousuquan island arc in the north (W.M. Li et al., 2002, 2006; Wang et al., 2014).

Based on the crossite Sm–Nd isochron dating of the eclogites (ca. 347 Ma) and $^{40}Ar/^{39}Ar$ plateau ages of phengite (ca. 334 and 331 Ma) from an omphacite–phengite-bearing blueschist, which formed in a Paleozoic accretionary wedge on the southern side of the Yili–Central Tianshan (YCT) block, Gao and Klemd (2003) considered that the subduction of the South Tianshan Ocean plate (which separated the Tarim craton and the YCT block) may have been completely finished by the end of the Early Carboniferous (Fig. 15a, b). Furthermore, new zircon U–Pb age data of ca. 320 Ma for the South Tianshan eclogites indicate that collision of the Tarim craton and YCT block occurred during the Late Carboniferous (Su et al., 2010). This would be inconsistent with our results, which indicate the Late Carboniferous Bailingshan felsic-intermediate arc magmatism was still ongoing at ca. 320 Ma, if the Aqishan–Yamansu belt was assumed to be a product of northward subduction of the South Tianshan oceanic plate. Hence, the Kanggur oceanic plate is suggested to have continued to subduct below the YCT block from the north into the Late Carboniferous, with the subduction-related arc and back-arc system forming on the northern side of the block (W.M. Li et al., 2002, 2006; Wang et al., 2014; Fig. 15a, b). This model is supported by: (1) Ophiolites along the Kanggur Fault representing remnants of the Kanggur oceanic plate (Li et al., 2006); (2) inherited zircons from the felsic volcanic rocks in the Yamansu Formation (ca. 348–334 Ma) that have similar age peaks (ca. 900 Ma and 1400 Ma) to the YCT block basement rocks (Luo et al., 2012), indicating that the Aqishan–Yamansu belt was possibly developed on the northern margin of the YCT block; (3) The Yamansu Formation underlies the northern part of the Aqishan–Yamansu belt, whereas the Late Carboniferous Tugutublak Formation (ca. 324 Ma; this study) is exposed in the southern part (Muhetaer et al., 2014), indicating a south-dipping subduction along the Yamansu Fault, consistent with typical subduction processes along continental margin arcs (Villagómez et al., 2011).

Qin et al. (2002) documented that the Yamansu Formation contains exceptionally thick (5 km) bimodal volcanic sequences, and Wang et al. (2006) reported that the Yinbangshan Cu deposit is a typical VMS deposit (Fig. 1b). These observations indicate a possible back-arc (or intra-arc) basin (Fig. 15a). Our geochemical data of the tuffaceous dacite and Bailingshan granitoids suggest that they were formed through juvenile crustal-derived melt with an increasing involvement of mantle-derived components by time (Fig. 14a–b). These features are similar to those of the Jurassic–Cretaceous batholiths distributed along the Central Andean coastal area (normally called the “Coastal Batholiths” in the Andes) (Fig. 14c–d), with a tectonic regime unambiguously dominated by back (intra)-arc basin–arc transition. These Central Andean batholiths are widely accepted to be dominantly generated by the remelting of isotopically juvenile crust (e.g., back-arc basin basaltic rocks) and mixing with minor mantle components during basin inversion (Atherton, 1990; Polliand et al., 2005; De Haller et al., 2006; Mišković and Schaltegger, 2009; Boekhout et al., 2012; Cochrane et al., 2014).

We infer that such a tectonic transition process may have also happened in the Late Carboniferous Aqishan–Yamansu Belt (e.g., at Bailingshan), as supported by not only the geochemical similarities between the Bailingshan granitoids and the Central Andean Coastal Batholiths, but also: (1) The Early Carboniferous Yamansu Formation contains mainly submarine bimodal arc volcanic–sedimentary strata, whereas the Late Carboniferous rocks are mainly intermediate-felsic Tugutublak Formation volcanic rocks and Bailingshan granitoids, all consistent with the lithologic association distributed along the Central Andean coastal area, in which more felsic rocks occurred during the basin inversion (Villagómez et al., 2011); (2) a number of arc-related skarn-like Fe and Cu deposits are distributed along the Aqishan–Yamansu belt, consistent with skarn Fe and iron oxide Cu–Au (IOCG) systems occurring in Andean districts that host the El Romeral, Monterrosas, and Carmen skarn-like Fe deposits (Bookstrom, 1977; Injoque et al., 1995; Injoque, 2002), and the Candelaria and Mantoverde IOCG deposits (Marschik and Fontboté, 2001; Benavides et al., 2007; Chen et al., 2010); (3) zircon U–Pb dating on gabbros at the Xiangshan Ni–Cu–Co deposit, representing products of the syn- to post-accretionary regime, has yielded an age of 279.6 Ma (Han et al., 2010). Moreover, $^{40}Ar/^{39}Ar$ plateau ages of biotite (ca. 290–270 Ma) for post-subduction movement along large-scale ductile shear zones in the Kanggur area (Xiao et al., 2004) indicate that the Kanggur Ocean was closed no later than the late Early Permian. The accelerated closure of the Kanggur Ocean towards the south may have caused the back (intra)-arc basin inversion in the Aqishan–Yamansu Belt (Fig. 15b).

To summarize, we infer that the Aqishan–Yamansu back (intra)-arc extension and subsequent basin inversion was formed in response to the south-dipping subduction of the Kanggur oceanic plate beneath the YCT block. Published and new LA-ICPMS zircon U–Pb ages of the felsic-intermediate rocks at Bailingshan indicate that the arc-related basin was closed ca. 325–300 Ma.

7. Conclusions

(1) Zircon U–Pb dating of the Bailingshan felsic-intermediate rocks has indicated ages for tuffaceous dacitic lava of 324.1 ± 2.1 Ma, granodiorite of 317.7 ± 1.8 Ma, monzonitic granite of 313.7 ± 2.1 Ma, and granite of 307.2 ± 2.3 Ma. These results suggest that the Bailingshan granitic intrusion occurred soon after the eruption of the Tugutublak dacite and the associated Fe skarns formed during the Late Carboniferous.

(2) Petrological and geochemical data indicate that the dacite and I-type granitoids belong to metaluminous calc-alkaline to high-K calc-alkaline series. The dacite and granite were likely to be derived from the melting of a juvenile lower crust mixed with some mantle-derived materials, and the mantle components may have played an increasingly more prominent role over time.

(3) Our geochemical study supports that the Aqishan–Yamansu back-arc basin extension took place during the south-dipping subduction of the Kanggur oceanic plate beneath the Yili–Central Tianshan block, with the felsic-intermediate magmatism occurring during back (intra)-arc basin inversion, similar to the Mesozoic Coastal Batholiths in the Central Andes.

Acknowledgments

This study was financially supported by the Chinese National Basic Research 973-Program (2014CB440802). We thank Wanjian Lu, Yunfeng Wang, Xuelu Yan, Bing Xiao, and Juntao Yang for their assistance with the field work. We are grateful to Chongyin Li for her assistance with the LA-ICPMS zircon U–Pb dating, and Chao Wu and Hongjun Jiang for the LA-MC-ICPMS zircon Hf isotope analyses. Our thanks go also to Jing Fang and Chenming Wang for their constructive comments in enhancing the manuscript. We thank Richard Goldfarb and two anonymous reviewers for their helpful and constructive reviews, which led to further improvement of the manuscript. This is contribution from GIGCAS No. IS-2158.

References

Atherton, M.P., 1990. The Coastal Batholith of Peru: the product of rapid recycling of ‘new’ crust formed within rifted continental margin. Geological Journal 25, 337–349.

Belousova, E., Griffin, W.L., O'Reilly, S.Y., Fisher, N.L., 2002. Igneous zircon: trace element composition as an indicator of source rock type. Contributions to Mineralogy and Petrology 143, 602–622.

Benavides, G.A., Squadrito, G.L., Mills, R.W., Patel, H.D., Isbell, T.S., Patel, R.P., Kraus, D.W., 2007. Hydrogen sulfide mediates the vasoactivity of garlic. Proceedings of the National Academy of Sciences 104, 17977–17982.

Boekhout, F., Spikings, R., Sempere, T., Chiaradia, M., Ulianov, A., Schaltegger, U., 2012. Mesozoic arc magmatism along the southern Peruvian margin during Gondwana breakup and dispersal. Lithos 146, 48–64.

Bookstrom, A.A., 1977. The magnetite deposits of El Romeral, Chile. Economic Geology 72, 1101–1130.
Bouvier, A., Vervoort, J.D., Patchett, P.J., 2008. The Lu–Hf and Sm–Nd isotopic composition of CHUR: constraints from unequilibrated chondrites and implications for the bulk composition of terrestrial planets. Earth and Planetary Science Letters 273, 48–57.
Boynton, W.V., 1984. Geochemistry of the rare earth elements: meteorite studies. In: Henderson, P. (Ed.), Rare Earth Element Geochemistry. Elsevier, Amsterdam, pp. 63–114.
Buick, R., Thornett, J.R., Mcnaughton, N.J., Smith, J.B., Barley, M.E., Savage, M., 1995. Record of emergent continental crust similar to 3.5 billion years ago in the Pilbara craton of Australia. Nature 375, 574–575.
Chappell, B.W., 1999. Aluminum saturation in I- and S-type granites and the characterization of fractionated haplogranites. Lithos 46, 535–551.
Chappell, B.W., White, A.J.R., 1974. Two contrasting granite types. Pacific Geology 8, 173–174.
Chappell, B.W., White, A.J.R., 1992. I- and S-type granites in the Lachlan Fold Belt. Geological Society of America Special Papers 272, 1–26.
Chappell, B.W., White, A.J.R., 2001. Two contrasting granite types: 25 years later. Australian Journal of Earth Sciences 48, 489–499.
Chen, Y.J., 2000. Progress in the study of Central Asia-type orogenesis–metallogenesis in northwest China. Geological Journal of China Universities 6, 17–22 (in Chinese with English abstract).
Chen, B., Jahn, B.M., 2004. Genesis of post-collisional granitoids and basement nature of the Junggar Terrane, NW China: Nd–Sr isotope and trace element evidence. Journal of Asian Earth Sciences 23, 691–703.
Chen, H.Y., Clark, A.H., Kyser, T.K., Ullrich, T.D., Baxter, R., Chen, Y., Moody, T.C., 2010. Evolution of the giant Marcona–Mina Justa iron oxide–copper–gold district, south-central Peru. Economic Geology 105, 155–185.
Chen, Y.J., Pirajno, F., Wu, G., Qi, J.P., Xiong, X.L., 2012. Epithermal deposits in North Xinjiang, NW China. International Journal of Earth Sciences 101, 889–917.
Chen, X.J., Shu, L.S., Santosh, M., Zhao, X.X., 2013. Island arc-type bimodal magmatism in the eastern Tianshan Belt, Northwest China: geochemistry, zircon U–Pb geochronology and implications for the Paleozoic crustal evolution in Central Asia. Lithos 168, 48–66.
Chu, N.C., Taylor, R.N., Chavagnae, V., Nesbitt, R.W., Boela, R.M., Milton, J.A., German, C.R., Bayon, G., Burton, K., 2002. Hf isotope ratio analysis using multi-collector inductively coupled plasma mass spectrometry: an evaluation of isobaric interference corrections. Journal of Analytical Atomic Spectrometry 17, 1567–1574.
Cochrane, R., Spikings, R., Gerdes, A., Winkler, W., Ulianov, A., Mora, A., Chiaradia, M., 2014. Distinguishing between in-situ and accretionary growth of continents along active margins. Lithos 202, 382–394.
De Haller, A., Corfu, F., Fontboté, L., Schaltegger, U., Barra, F., Chiaradia, M., Frank, M., Alvarado, J.Z., 2006. Geology, geochronology, and Hf and Pb isotope data of the Raúl–Condestable iron oxide–copper–gold deposit, central coast of Peru. Economic Geology 101, 281–310.
Defant, M.J., Drummond, M.S., 1990. Derivation of some modern arc magmas by melting of young subducted lithosphere. Nature 347, 662–665.
Eby, G.N., 1992. Chemical subdivision of the A-type granitoids: petrogenetic and tectonic implications. Geology 20, 641–644.
Gao, J., Klemd, R., 2003. Formation of HP–LT rocks and their tectonic implications in the western Tianshan Orogen, NW China: geochemical and age constraints. Lithos 66, 1–22.
Green, T.H., 1995. Significance of Nb/Ta as an indicator of geochemical processes in the crust–mantle system. Chemical Geology 120, 347–359.
Griffin, W.L., Wang, X., Jackson, S.E., Pearson, N.J., O'Reilly, S.Y., Xu, X.S., Zhou, X.M., 2002. Zircon chemistry and magma mixing SE China: in-situ analysis of Hf isotopes. Tonglu and Pingtan igneous complexes. Lithos 61, 237–269.
Griffin, W.L., Belousova, E.A., Shee, S.R., Pearson, N.J., O'Reilly, S.Y., 2004. Archean crustal evolution in the northern Yilgarn Craton: U–Pb and Hf-isotope evidence from detrital zircons. Precambrian Research 13l, 23l–282l.
Han, J.W., Ma, Z.D., 2003. Isotope geochemistry. In: Ma, Z.D., Zhang, H.F. (Eds.), GeochemistrySpecial Publication 225. Geology Publishing House, Beijing, pp. 213–266.
Han, C.M., Xiao, W.J., Zhao, G.C., Ao, S., Zhang, J., Qu, W., Du, A., 2010. In-situ U–Pb, Hf and Re–Os isotopic analyses of the Xiangshan Ni–Cu–Co deposit in Eastern Tianshan (Xinjiang), Central Asia Orogenic Belt: constraints on the timing and genesis of the mineralization. Lithos 120, 547–562.
Han, C.M., Xiao, W.J., Zhao, G.C., Su, B.X., Sakyi, P.A., Ao, S., Wan, B., Zhang, J., Zhang, Z.Y., 2014. Late Paleozoic metallogenesis and evolution of the East Tianshan Orogenic Belt (NW China, Central Asia Orogenic Belt). Geology of Ore Deposits 56, 493–512.
Hou, Z.Q., Zheng, Y.C., Yang, Z.M., Rui, Z.Y., Zhao, Z.D., Jiang, S.H., Qu, X.M., Sun, Q.Z., 2013. Contribution of mantle components within juvenile lower-crust to collisional zone porphyry Cu systems in Tibet. Mineralium Deposita 48, 173–192.
Hou, T., Zhang, Z.C., Santosh, M., Encarnacion, J., Zhu, J., Luo, W.Q., 2014. Geochronology and geochemistry of submarine volcanic rocks in the Yamansu iron deposit, Eastern Tianshan Mountains, NW China: constraints on the metallogenesis. Ore Geology Reviews 56, 487–502.
Huang, X.W., Qi, L., Gao, J.F., Zhou, M.F., 2013. First reliable Re–Os ages of pyrite and stable isotope compositions of Fe (–Cu) deposits in the Hami Region, Eastern Tianshan Orogenic Belt, NW China. Resource Geology 63, 166–187.
Injoque, J., 2002. Fe oxide–Cu–Au deposits in Peru: an integrated view. Hydrothermal iron oxide copper–gold and related deposits: a global perspective. 2, 97–113.
Injoque, J., Valera, J., Miranda, C., 1995. Geología del Distrito Minero de Cata Cañete, Aspectos Petrológicos y Estructurales con Mención en la Mineralización de Cobre. Bol. Sociedad Geológica del Perú 84 pp. 43–78.
Jahn, B.M., Zhang, Z.Q., 1984. Archean granulite gneisses from eastern Hebei Province, China: rare earth geochemistry and tectonic implications. Contributions to Mineralogy and Petrology 85, 224–243.
Kemp, A.I.S., Hawkesworth, C.J., Foster, G.L., Paterson, B.A., Woodhead, J.D., Hergt, J.M., Gray, C.M., Whitehouse, M.J., 2007. Magmatic and crustal differentiation history of granitic rocks from hafnium and oxygen isotopes in zircon. Science 315, 980–983.
Kinny, P.D., Maas, R., 2003. Lu–Hf and Sm–Nd isotope systems in zircon. In: Hanchar, J.M., Hoskin, P.W.O. (Eds.), Zircon Reviews in Mineralogy and Geochemistry 53, pp. 327–341.
Lei, R.X., Wu, C.Z., Zhang, Z.Z., Gu, L.X., Tang, J.H., Li, G.R., 2013. Geochronology, geochemistry and tectonic significances of the Yamansubei pluton in eastern Tianshan, Northwest China. Acta Petrologica Sinica 29, 2653–2664.
Li, C.M., 2009. A review on the minerageny and situ microanalytical dating techniques of zircons. Geological Survey and Research 33, 161–174 (in Chinese with English abstract).
Li, X.J., Li, X.H., 1999. Geology and metallogenesis of the Bailingshan iron deposit in Shanshan, Xingjiang. Geology and Prospecting 3, 9–14 (in Chinese with English abstract).
Li, J.Y., Wang, K.Z., Li, W.Q., Guo, H.C., Song, B., Wang, Y., Mo, S.G., Zhao, Z.R., Zhu, Z.X., Pan, C.Z., 2002a. Tectonic evolution since the Late Paleozoic and mineral prospecting in Eastern Tianshan Mountains, NW China. Xinjiang Geology 20, 295–301 (in Chinese with English abstract).
Li, W.M., Ren, B.Z., Yang, X.K., Li, Y.Z., Chen, Q., 2002b. The intermediate-acid intrusive magmatism and its geodynamic significance in Eastern Tianshan region. Northwestern Geology 35, 41–64 (in Chinese with English abstract).
Li, J.Y., Wang, K.Z., Sun, G.H., Mo, S.G., Li, W.Q., Yang, T.N., Gao, L.M., 2006. Paleozoic active margin slices in the southern Turfan–Hami basin: geological records of subduction of the Paleo-Asian ocean plate in Central Asian regions. Acta Petrologica Sinica 22, 1087–1102 (in Chinese with English abstract).
Li, H., Zhang, H., Ling, M.X., Wang, F.Y., Ding, X., Zhou, J.B., Yang, X.Y., Tu, X.L., Sun, W.D., 2011. Geochemical and zircon U–Pb study of the Huangmeijian A-type granite: implications for geological evolution of the Lower Yangtze River belt. International Geology Review 53, 499–525.
Li, L., Yi, A.W., Bu, H.Y., 2012. Geological characteristics and prospecting marks of the Yingbangshan deposit, Hami, Xingjiang, China. Science and Technology Information 5, 533–534 (in Chinese).
Liang, X.R., Wei, G.J., Li, X.H., Liu, Y., 2003. Precise determination of $^{143}Nd/^{144}Nd$ and Sm/Nd isotopes using MC-ICPMS. Geochimica 32, 91–96.
Liew, T.C., Hofmann, A.W., 1988. Precambrian crustal components, plutonic associations, plate environment of the Hercynian Fold Belt of central Europe: indications from a Nd and Sr isotopic study. Contributions to Mineralogy and Petrology 98, 129–138.
Liu, Y.S., Hu, Z.C., Gao, S., Günther, D., Xu, J., Gao, C.G., Chen, H.H., 2008. In-situ analysis of major and trace elements of anhydrous minerals by LA-ICP-MS without applying an internal standard. Chemical Geology 257, 34–43.
Ludwig, K.R., 2003. ISOPLOT 3.00: A Geochronological Toolkit for Microsoft Excel. Berkeley Geochronology Center, Berkeley, California (BGC Special Publication, Berkeley).
Lugmair, G.W., Harti, K., 1978. Lunar initial $^{143}Nd/^{144}Nd$: differential evolution of the lunar crust and mantle. Earth and Planetary Science Letters 39, 349–357.
Luo, T., Liao, A.Q., Chen, J.P., Zhang, X.H., Guo, D.B., Hu, Z.C., 2012. LA-ICP-MS zircon U–Pb dating of the volcanic rocks from Yamansu Formation in the Eastern Tianshan, and its geological significance. Earth Science-Journal of China University of Geosciences 6, 1338–1352 (in Chinese with English abstract).
Machado, N., Simonetti, A., 2001. U–Pb dating and Hf isotopic composition of zircon by laser-ablation-MC-ICP-MS. In: Sylvester, P. (Ed.), Mineralogical Association of Canada, Canada, Special Publication, pp. 121–146.
Maniar, P.D., Piccoli, P.M., 1989. Tectonic discrimination of granitoids. Geological Society of America Bulletin 101, 635–643.
Mao, J.W., Goldfarb, R.J., Wang, Y., Hart, C.J., Wang, Z., Yang, J., 2005. Late Paleozoic base and precious metal deposits, East Tianshan, Xinjiang, China: characteristics and geodynamic setting. Episodes-Newsmagazine of the International Union of Geological Sciences 28, 23–30.
Marschik, R., Fontboté, L., 2001. The Candelaria-Punta del Cobre iron oxide Cu–Au (–Zn–Ag) deposits, Chile. Economic Geology 96, 1799–1826.
McCulloch, M.T., Gamble, J.A., 1991. Geochemical and geodynamical constraints on subduction zone magmatism. Earth and Planetary Science Letters 102, 358–374.
McKenzie, D., 1989. Some remarks on the movement of small melt fractions in the mantle. Earth and Planetary Science Letters 95, 53–72.
Meng, Q.P., Cai, F.M., Liu, F., Gen, X.X., Han, W.Q., 2013. Rare earth element tracer of the Bailingshan iron deposit, Eastern Tianshan. Acta Mineralogica Sinica 603–604 (in Chinese).
Mišković, A., Schaltegger, U., 2009. Crustal growth along a non-collisional cratonic margin: a Lu–Hf isotopic survey of the Eastern Cordilleran granitoids of Peru. Earth and Planetary Science Letters 279, 303–315.
Muhetaer, Z., Nijat, A., Wu, Z., 2014. Geochemical characteristics of volcanics from the Southern Jueluotage Area and their constraints on the tectonic of Paleo-Asian Ocean. Earth Science Frontiers 21, 1–13 (in Chinese with English abstract).
Müller, D., Rock, N.M.S., Groves, D.I., 1992. Geochemical discrimination between shoshonitic and potassic volcanic rocks in different tectonic settings: a pilot study. Mineralogy and Petrology 46, 259–289.
Pearce, J.A., Cann, J.R., 1973. Tectonic setting of basic volcanic rocks determined using trace element analyses. Earth and Planetary Science Letters 19, 290–300.
Pearce, J.A., Peate, D.W., 1995. Tectonic implications of the composition of volcanic arc magmas. Annual Review of Earth and Planetary Sciences 23, 251–285.
Peccerillo, A., Taylor, S.R., 1976. Geochemistry of Eocene calc-alkaline volcanic rocks from the Kastamonu area, northern Turkey. Contributions to Mineralogy and Petrology 58, 63–81.

Pirajno, F., Seltmann, R., Yang, Y.Q., 2011. A review of mineral systems and associated tectonic settings of northern Xinjiang, NW China. Geoscience Frontiers 2, 157–185.
Pitcher, W.S., 1993. The Nature and Origin of Granite 321. Chapman and Hall, Special Publication, London, pp. 316–338.
Polliand, M., Schaltegger, D., Frank, U., Fontbote, N., 2005. Formation of intra-arc volcanosedimentary basins in the western flank of the central Peruvian Andes during Late Cretaceous oblique subduction: field evidence and constraints from U–Pb ages and Hf isotopes. International Journal of Earth Sciences 94, 231–242.
Qin, K.Z., 2000. Metallogenesis in relation to central-Asia style orogeny of northern Xinjiang. Institute of Geology and Geophysics, Chinese Academy of Science, Beijing, Unpublished Postdoctoral Research Report. (230 pp. (in Chinese with English abstract)).
Qin, K.Z., Fang, T.H., Wang, S.L., Zhu, B.Q., Feng, Y.M., Yu, H.F., Xiu, Q.Y., 2002. Plate tectonics division, evolution and metallogenic settings in eastern Tianshan Mountains, NW China. Xinjiang Geology 20, 302–308 (in Chinese with English abstract).
Qin, K.Z., Peng, X.M., San, J.Z., Xu, X.W., Fang, T.H., Wang, S.L., Yu, H.F., 2003. Types of major ore deposits, division of metallogenic belts in eastern Tianshan, and discrimination of potential prospects of Cu, Au, Ni mineralization. Xinjiang Geology 21, 143–150 (in Chinese with English abstract).
Rapp, R.P., Watson, E.B., 1995. Dehydration melting of metabasalt at 8–32 kbar: implications for continental growth and crust–mantle recycling. Journal of Petrology 36, 891–931.
Richards, J.P., Kerrich, R., 2007. Special paper: adakite-like rocks: their diverse origins and questionable role in metallogenesis. Economic Geology 102, 537–576.
Rui, Z.Y., Wang, L.S., Wang, Y.T., Liu, Y.L., 2002. Discussion on metallogenic epoch of Tuwu and Yandong porphyry copper deposits in Eastern Tianshan Mountains, Xinjiang. Mineral Deposits 21, 16–22.
Sang, S.J., Peng, M.X., Guo, Y.H., 2003. Optimized Target Areas and Evaluation Report of Resource in the Caixiashan to Jintan Area. Xingjiang institute of Geology Investigation, pp. 42–44.
Santosh, M., Yang, Q., Shaji, E., Tsunogae, T., RamMohan, M., Satyanarayanan, M., 2015. An exotic Mesoarchean microcontinent: the Coorg Block, southern India. Gondwana Research 27, 165–195.
Sengör, A.M.C., Natal'in, B.A., 1996. Paleotectonics of Asia: fragments of synthesis. In: Yin, A., Harrison, T.M. (Eds.), The Tectonic Evolution of Asia. Cambridge University Press, Cambridge, pp. 486–640 (Special Publication).
Sengör, A.M.C., Natal'in, B.A., Burtman, V.S., 1993. Evolution of the Altaid tectonic collage and Paleozoic crustal growth in Asia. Nature 364, 299–307.
Smithies, R.H., Champion, D.C., 2000. The Archaean high-Mg diorite suite: links to tonalite–trondhjemite–granodiorite magmatism and implications for Early Archaean crustal growth. Journal of Petrology 41, 1653–1671.
Soderlund, U., Patchett, P.J., Vervoort, J.D., Isachsen, C.E., 2004. The ^{176}Lu decay constant determined by Lu–Hf and U–Pb isotope systematics of Precambrian mafic intrusions. Earth and Planetary Science Letters 219, 311–324.
Song, A.J., Zhu, Z.X., Shi, Y., Li, S.H., 2006. SHRIMP U–Pb dating of zircons from the Tugutu Bulake Formation in the western segment of the Aqikkuduke fault in the Eastern Tianshan, Xingjiang, China. Geological Bulletin of China 25, 953–956 (in Chinese with English abstract).
Steiger, R.H., Jäger, E., 1977. Subcommission on geochronology; convention on the use of decay constants in geochronology and cosmochronology. Earth and Planetary Science Letters 36, 359–362.
Su, W., Gao, J., Klemd, R., Li, J.L., Zhang, X., Li, X.H., Chen, N.S., Zhang, L., 2010. U–Pb zircon geochronology of Tianshan eclogites in NW China: implication for the collision between the Yili and Tarim blocks of the southwestern Altaids. European Journal of Mineralogy 22, 473–478.
Sun, S.S., McDonough, W.F., 1989. Chemical and isotopic systematics of oceanic basalts: implications for mantle composition and processes. In: Saunders, A.D., Norry, M.J. (Eds.), Magmatism in the Ocean Basins. Geological Society, London, Special Publications 42, pp. 313–345.
Vervoort, J.D., Blichert-Toft, J., 1999. Evolution of the depleted mantle: Hf isotope evidence from juvenile rocks through time. Geochimica et Cosmochimica Acta 63, 533–556.
Villagómez, D., Spikings, R., Magna, T., Kammer, A., Winkler, W., Beltrán, A., 2011. Geochronology, geochemistry and tectonic evolution of the Western and Central cordilleras of Colombia. Lithos 125, 875–896.
Wang, L.S., Li, H.Q., Chen, Y.C., Liu, D.Q., 2005. Geological feature and mineralization epoch of Bailingshan iron deposit, Hami, Xingjiang, China. Mineral Deposits 24, 280–284 (in Chinese with English abstract).
Wang, J.B., Wang, Y.W., He, Z.J., 2006. Ore deposits as a guide to the tectonic evolution in the East Tianshan Mountains, NW China. Geology in China 33, 461–469 (in Chinese with English abstract).
Wang, Y.H., Xue, C.J., Liu, J.J., Wang, J.P., Yang, J.T., Zhang, F.F., Zhao, Z.N., Zhao, Y.J., Liu, B., 2014. Early Carboniferous adakitic rocks in the area of the Tuwu deposit, eastern Tianshan, NW China: slab melting and implications for porphyry copper mineralization. Journal of Asian Earth Sciences 103, 1–18.
Wei, G.J., Liang, X.R., Li, X.H., Liu, Y., 2002. Precise determination of Sr isotopes of solution and solid samples using LA-MC-ICPMS. Geochimica 31, 295–305.
Whalen, J.B., Currie, K.L., Chappell, B.W., 1987. A-type granites: geochemical characteristics, discrimination and petrogenesis. Contributions to Mineralogy and Petrology 95, 407–419.
Wilson, M., 1989. Igneous Petrogenesis — A global Tectonic Approach. Unwin Hyman, London, p. 466.
Winchester, J.A., Floyd, P.A., 1976. Geochemical magma type discrimination: application to altered and metamorphosed basic igneous rocks. Earth and Planetary Science Letters 28, 459–469.
Windley, B.F., Alexeiev, D., Xiao, W.J., Kröner, A., Badarch, G., 2007. Tectonic models for accretion of the Central Asian Orogenic Belt. Journal of the Geological Society 64, 31–47.
Woodhead, J.D., Hergt, J.M., Davidson, J.P., Eggins, S.M., 2001. Hafnium isotope evidence for 'conservative' element mobility during subduction zone processes. Earth and Planetary Science Letters 192, 331–346.
Wu, F.Y., Jahn, B.M., Wilde, S.A., Lo, C.H., Yui, T.F., Lin, Q., Ge, W.C., Sun, D.Y., 2003. Highly fractionated I-type granites in NE China (I): geochronology and petrogenesis. Lithos 66, 241–273.
Wu, C.Z., Zhang, Z.Z., Zaw, K., Della-Pasque, F., Tang, J.H., Zheng, Y.C., Wang, C.S., San, J.Z., 2006a. Geochronology, geochemistry and tectonic significances of the Hongyuntan granitoids in the Qoltag area, Eastern Tianshan. Acta Petrologica Sinica 22, 1121–1134 (in Chinese with English abstract).
Wu, F.Y., Yang, Y.H., Xie, L.W., Yang, J.H., Xu, P., 2006b. Hf isotopic compositions of the standard zircons and baddeleyites used in U–Pb geochronology. Chemical Geology 234, 105–126.
Xiao, W.J., Zhang, L.C., Qin, K.Z., Sun, S., Li, J.L., 2004. Paleozoic accretionary and collisional tectonics of the Eastern Tianshan (China): implications for the continental growth of Central Asia. American Journal of Science 304, 370–395.
Xiao, W.J., Han, C.M., Yuan, C., Sun, M., Lin, S.F., Chen, H.L., Li, Z.L., Li, J.L., Sun, S., 2008. Middle Cambrian to Permian subduction-related accretionary orogenesis of northern Xinjiang, NW China: implications for the tectonic evolution of Central Asia. Journal of Asian Earth Sciences 32, 102–117.
Xiao, W.J., Windley, B.F., Yuan, C., Sun, M., Han, C.M., Lin, S.F., Chen, H.L., Yan, Q.R., Liu, D.Y., Qin, K.Z., Li, J.L., Sun, S., 2009. Paleozoic multiple subduction-accretion processes of the southern Altaids. American Journal of Science 309, 221–270.
Xiao, W.J., Windley, B.E., Allen, M.B., Han, C.M., 2013. Paleozoic multiple accretionary and collisional tectonics of the Chinese Tianshan orogenic collage. Gondwana Research 23, 1316–1341.
Yang, X.K., Tao, H.X., Luo, G.C., Ji, J.S., 1996. Basic features of plate tectonics in Eastern Tianshan of China. Xinjiang Geology 14, 221–227.
Yang, F.Q., Mao, J.W., Bierlein, F.P., Pirajno, F., Zhao, C.S., Ye, H.S., Liu, F., 2009. A review of the geological characteristics and geodynamic mechanisms of Late Paleozoic epithermal gold deposits in North Xinjiang, China. Ore Geology Reviews 35, 217–234.
Yang, W.B., Niu, H.C., Shan, Q., Sun, W.D., Zhang, H., Li, N.B., Jiang, Y.H., Yu, X.Y., 2014. Geochemistry of magmatic and hydrothermal zircon from the highly evolved Baerzhe alkaline granite: implications for Zr–REE–Nb mineralization. Mineralium Deposita 49, 451–470.
Zhang, K.J., Zhang, M., 2012. The comprehensive application of mining method for the local and thick ore-body. Metal Mine 430, 51–53 (in Chinese with English abstract).
Zhang, L.C., Xiao, W.J., Qin, K.Z., Zhang, Q., 2006. The adakite connection of the Tuwu–Yandong copper porphyry belt, eastern Tianshan, NW China: trace element and Sr–Nd–Pb isotope geochemistry. Mineralium Deposita 41, 188–200.
Zhang, X.H., Huang, X., Chen, J.P., Liao, Q.A., Duan, X.F., 2012. Stratigraphic sequence of carboniferous marine volcanic-deposit rock and its geological age in Juotage Area, Eastern Tianshan. Earth Science-Journal of China University of Geosciences 6, 1305–1314 (in Chinese with English abstract).
Zhao, Z.H., Xiong, X.L., Wang, Q., Wyman, D.A., Bao, Z.W., Bai, Z.H., Qiao, Y.L., 2008. Underplating-related adakites in Xinjiang Tianshan, China. Lithos 102, 374–391.
Zhou, P.B., Mukasa, S.B., 1997. Nd–Sr–Pb isotopic, and major-and trace-element geochemistry of Cenozoic lavas from the Khorat Plateau, Thailand: sources and petrogenesis. Chemical Geology 137, 175–193.
Zhou, M.F., Lesher, M.C., Yang, Z.X., Li, J.W., Sun, M., 2004. Geochemistry and petrogenesis of 270 Ma Ni–Cu–(PGE) sulfide-bearing mafic intrusions in the Huangshan district, Eastern Xinjiang, Northwest China: implications for the tectonic evolution of the Central Asian orogenic belt. Chemical Geology 209, 233–257.
Zhou, T.F., Yuan, F., Zhang, D.Y., Fan, Y., Liu, S., Peng, M.X., Zhang, J.D., 2010. Geochronology, tectonic setting and mineralization of granitoids in Jueluotage area, eastern Tianshan, Xingjiang. Acta Petrologica Sinica 26, 478–520 (in Chinese with English abstract).